Chapter 4. Application to Cavity-Type Thermal Radiation Detectors

This chapter describes the numerical experiments carried out to validate the theoretical statistical protocol developed in Chapter 3. First, a description of the numerical experiments is provided. Then, the chapter is divided into sections according to the equation being validated.

The cavity analyzed in this section and shown in Figure 4.1 has been studied by the author in previous contributions [Mahan *et al.*, 1998; Sánchez *et al.*, 1999; Sánchez *et al.*, 2000]. This design was proposed to be used on the Geostationary Earth Radiation Budget (GERB) experiment. Although the design was not selected for use on GERB, it has been the subject of several studies due to its simplicity and efficiency in directing incident radiation to the detector. It consists of nine surfaces; seven of which are mirror-like surfaces with a high specularity ratio; one of which is a slit, or entrance aperture; and one of which is a surface with high absortivity that plays the role of the detector. Incident radiation is simulated to enter the cavity through the slit at the top and strike the blackened active junction of a thermopile, which acts as the detector. Weckmann [1997] reports complete documentation of the thermoelectric performance of the thermopiles. In her master's thesis the author [Sánchez, 1998] presents an optical model of the wedge-shaped cavity and uses the MCRT method to determine the optimal wedge angle β (= 45 deg) for the cavity. She also analyzes the optical "cross-talk" among the pixels of the detector. Sorensen [1998] integrated the optical MCRT model with an electrothermal finite element method model reported by Weckmann [1997] to create an end-to-end instrument model. He also developed an algorithm to correct for the optical "cross-talk."

Note that the actual dimensions of the cavity in Figure 4.1 are unimportant as long as the condition $\Delta\xi \equiv a(2/\lambda z)^{1/2} >> 1.0$ is met [Mahan, 2002]. In the figure a = 180.5 μm and z = 180.5 μm. Then an MCRT analysis is valid only in the ultraviolet, visible, and near infrared ($\lambda < 10$ μm), as explained in Chapter 5 of Mahan [2002].

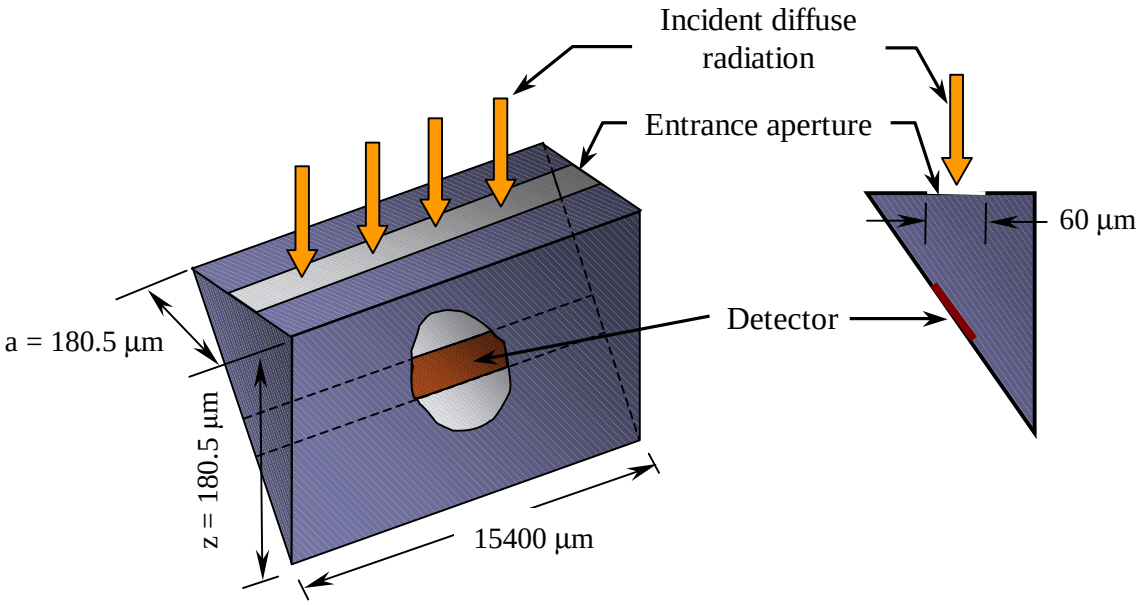

Figure 4.1 Schematic diagram of the cavity used in the numerical experiments (not to scale)

4.1 Description of numerical experiments

The MCRT-based software package FELIX was used to model the cavity and to perform the majority of the numerical experiments described in this chapter. Ten different numerical experiments, each one run with a different set of seeds for the integral random number generator, have been studied. Each experiment consists of executing the ray trace for different numbers of energy bundles.

After defining the optical properties of the cavity and introducing the geometry in FELIX, the program yields the distribution factor matrix for the nine surfaces. Figure 4.2 shows the numbering of the surfaces of the cavity. For example, D_{61} is the distribution factor from the entrance aperture to the detector. Table 4.1 shows the values of the optical

properties used in the ten experiments. The numerical experiments are used to establish the validity of Equations 3.5, 3.13, 3.24, and 3.39.

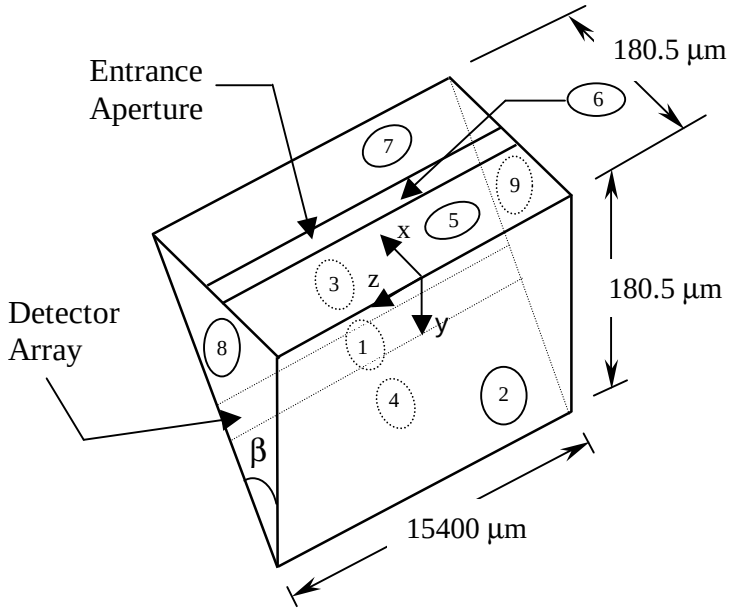

Figure 4.2 Division of the cavity in surfaces (not to scale)

Table 4.1 Optical properties of the cavity

Surface element number	Surface element name	Absorptivity α	Specularity ratio r_s
1	Detector	0.9	0.1
2	Mirrored wall	0.1	0.9
3	Mirrored wall	0.1	0.9
4	Mirrored wall	0.1	0.9
5	Mirrored wall	0.1	0.9
6	Entrance aperture	1	NA
7	Mirrored wall	0.1	0.9
8	Mirrored wall	0.1	0.9
9	Mirrored wall	0.1	0.9

4.2 Validation of Equation 3.5

The upper limit of the error of a single distribution factor between two specified surface elements is given by Equation 3.5,

$$Err_{D'_{ij}} \le W_c \sqrt{\frac{D'^{e}_{ij}(1-D'^{e}_{ij})}{N}} \tag{3.5}$$

where $Err_{D'_{ij}}$ is the difference between the "true" and estimated value of D'_{ij}, W_c is the critical value of the W statistic, N is the number of energy bundles, and D'^{e}_{ij} is the estimated value of the distribution factor from surface element i to surface element j.

In order to establish the validity of Equation 3.5 the numerical experiments were carried out for one thousand, ten thousand, one hundred thousand, one million, ten million, and one hundred million energy bundles emitted from each surface, each one producing a different distribution factor matrix. In the majority of the studies the most important distribution factor is the one from the entrance aperture to the detector; therefore, the distribution factor D'_{61} has been singled out to demonstrate the validity of Equation 3.5. A "true"[1] value is necessary to calculate the magnitude of the error of the distribution factors. First, collimated radiation entering the cavity through the slit normal to the plane of the slit was modeled to perform a convergence analysis. Figures 4.3 and 4.4 illustrate the convergence of the distribution factor D'_{61} with the number of energy bundles traced for collimated radiation entering the cavity.

In Figure 4.3 it is possible to see that the distribution factor D'_{61} begins to converge to an acceptable accuracy when one hundred thousand energy bundles have entered the cavity through the slit. Figure 4.4 shows the percent difference, $(\Delta D'_{61}/\Delta \log_{10} N)\times 100\%$, between consecutive distribution factors of Figure 4.3. The value of the percent difference for a billion of energy bundles is 0.00263. It is clear that the difference goes essentially to zero as the number of energy bundles increases, thus illustrating the convergence of the distribution factors as N becomes sufficiently large. Although it is possible to conclude that convergence is reached at a hundred thousand energy bundles, the value of the distribution factor corresponding to a hundred million is arbitrarily chosen as the "true" value.

[1] Remember that the exact value for the true distribution factor can only be obtained by tracing an infinite number of energy bundles.

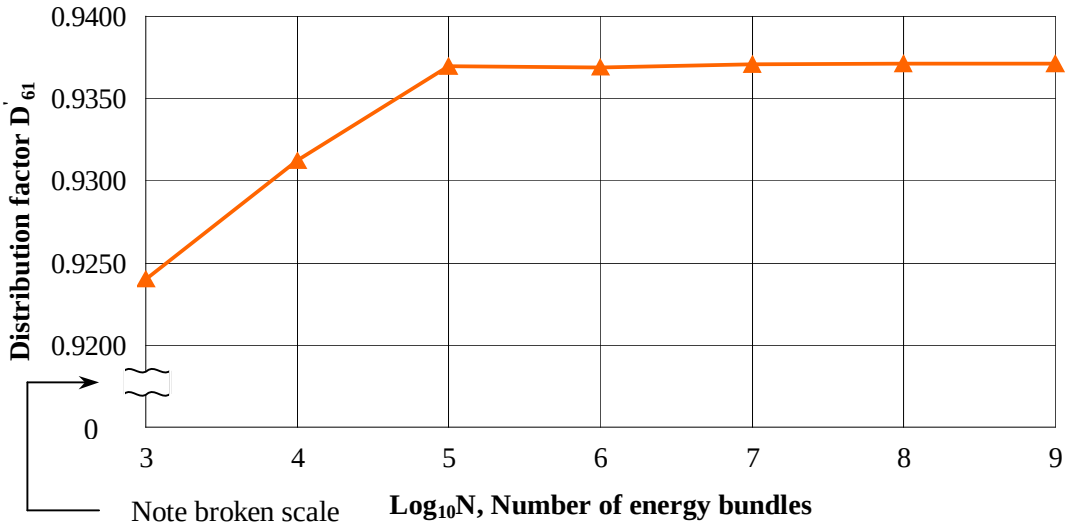

Figure 4.3 Convergence of distribution factor D'_{61} from the entrance aperture to the detector with collimated radiation entering the cavity normal to the plane of the slit

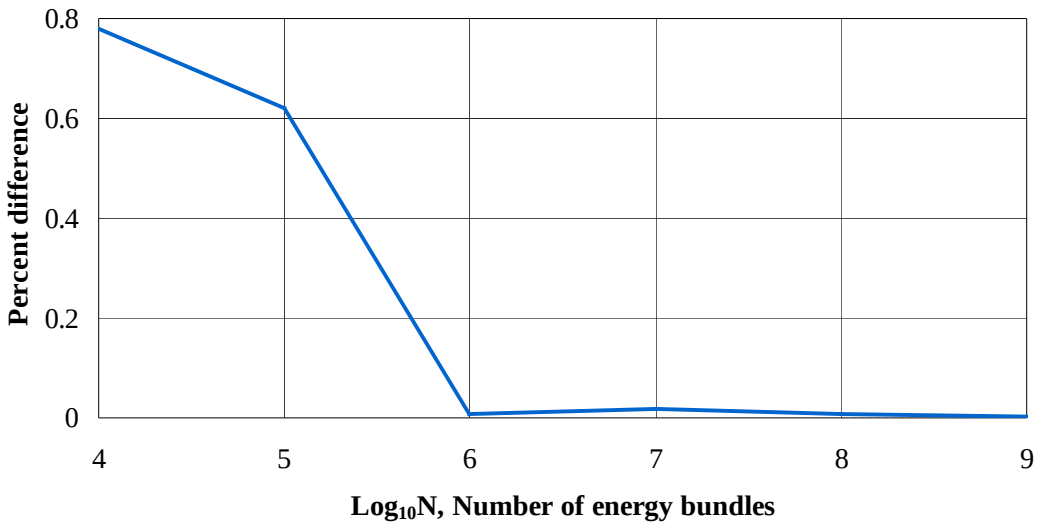

Figure 4.4 Percent difference of distribution factors with increasing number of energy bundles

From this point forward it is assumed that all the surfaces of the cavity emit radiation diffusely. It is shown throughout this chapter that a hundred million rays still provide a good estimate for a "true" value. The magnitude of the difference between the estimated value and the "true" value is calculated after the estimated value of the distribution factor D'_{61} has been obtained from FELIX. This difference is then compared to the value obtained using the right-hand side of Equation 3.5. Figure 4.5 shows the results of this comparison for three different numerical experiments chosen arbitrarily because of their typical behavior (in this case, experiments 1, 3, and 5).

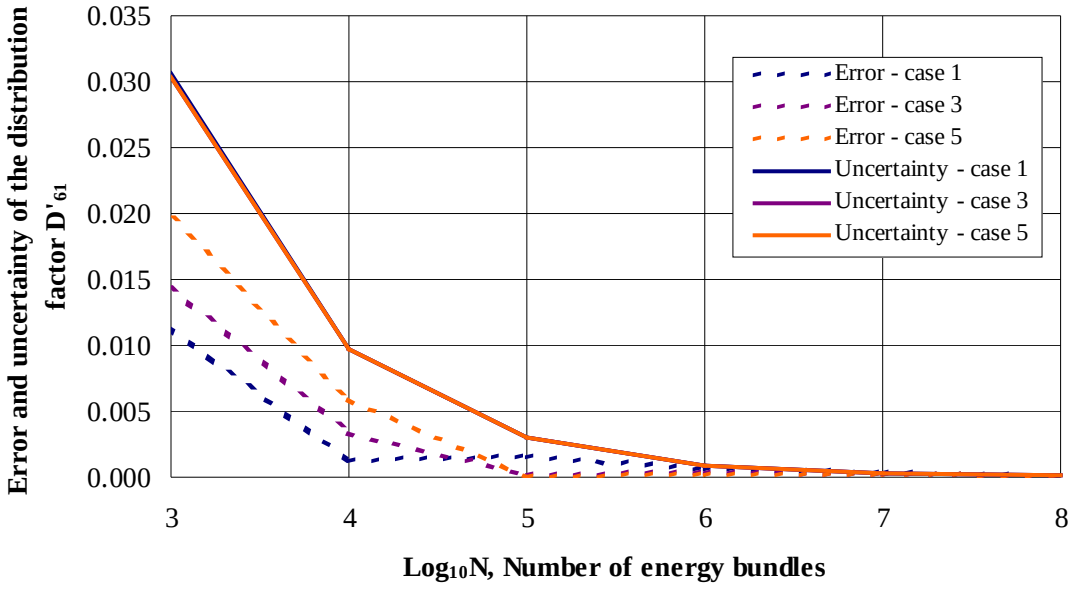

Figure 4.5 Magnitude of the error and uncertainty of distribution factor D'_{61} as predicted using Equation 3.5 and obtained from three numerical experiments

In Figure 4.5 it is clear that the left-hand side of Equation 3.5 (error of the distribution factor D'_{61}) from numerical experiments as well as the values of the right-hand side (uncertainty of the distribution factor D'_{61}) approach each other as the number of energy bundles increases. Also note that the solid curves, which represent the right-hand side of Equation 3.5, are almost identical. This can be explained by the behavior of the term $D'_{ij}(1-D'_{ij})$, typical of proportions and representative of the distribution factors.

As D'_{ij} becomes smaller, $(1 - D'_{ij})$ becomes larger. Also as expected the curves corresponding to Equation 3.5 form an upper bound for all the numerical experiments.

A study was made of the difference between the values obtained using the right-hand side of Equation 3.5 and the numerical experiments. Figures 4.6 and 4.7 show the result of this study. Recall that the difference between any two numerical experiments occurs because of the difference in the set of values of the initial seed used to generate the sequence of random number used. In Figure 4.6, the magnitude of the difference between the error of the distribution factors (left-hand side of Equation 3.5), and its uncertainty (right-hand side) is plotted for each number of energy bundles traced. In Figure 4.7 the mean of the differences of the ten numerical experiments is plotted with the corresponding 95-percent confidence interval.

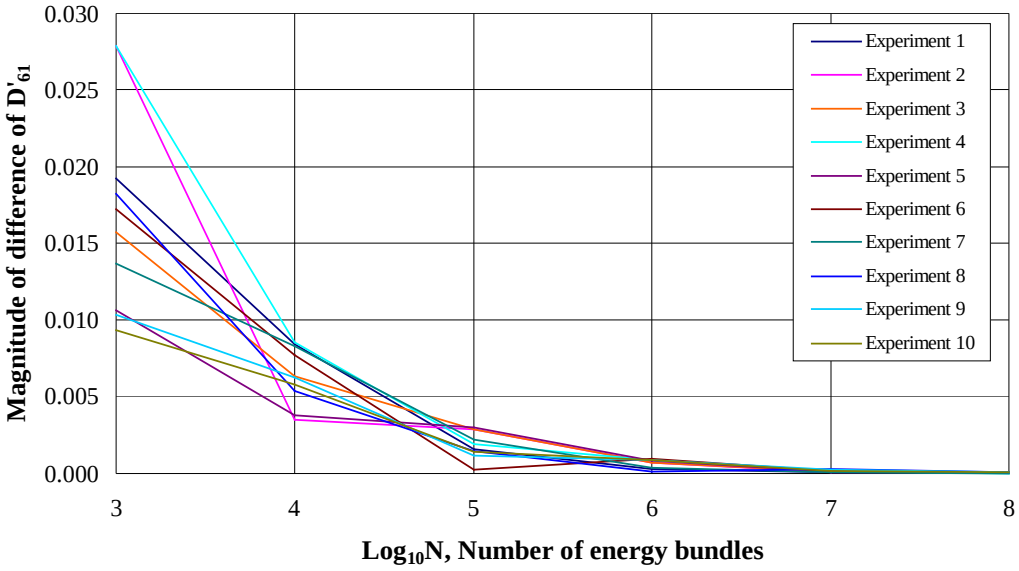

Figure 4.6 Magnitude of the difference between the error and the uncertainty of the distribution factor D'_{61} ("true" value of D'_{61} = 0.4126157)

In Figures 4.5 through Figure 4.7 a nominal value of 0.4126157 is used as the "true" value of the distribution factor D'_{61} corresponding to hundred million energy bundles traced. In both figures it is clear that the difference gets smaller as the number of energy bundles increases, which is in agreement with Equation 3.5. Note that the range of values of the differences for a thousand energy bundles in Figure 4.6 is very large as is

the value of the confidence interval. This means that a thousand energy bundles per surface element would significantly under-sample this particular cavity.

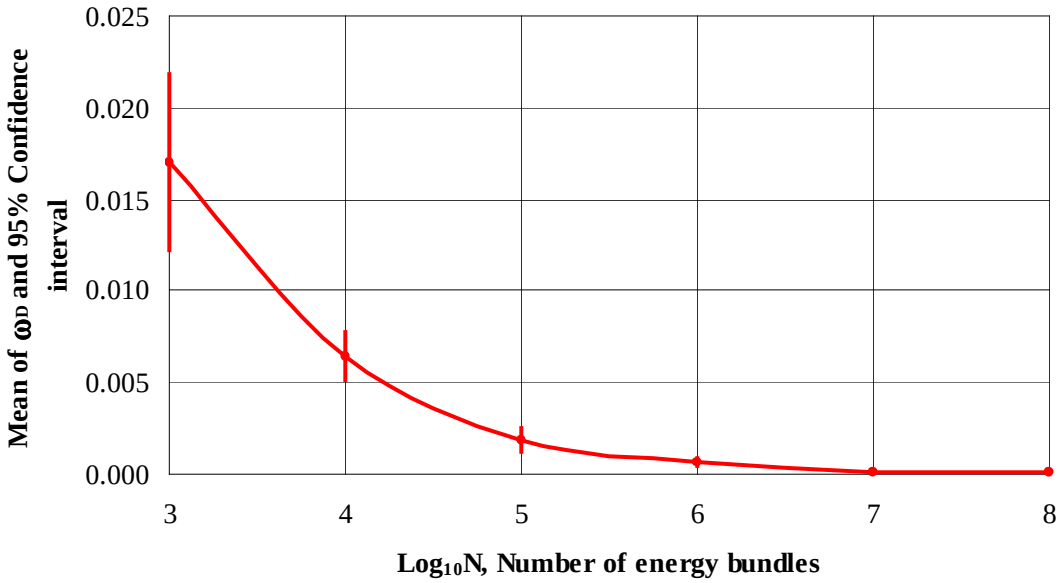

Figure 4.7 Mean of the difference between experimental and theoretical values of D'_{61} and their corresponding 95-percent confidence interval

4.3 Validation of Equation 3.13

Equation 3.13, repeated below, is a very important result of the current investigation. It relates the global distribution factor error, $Err_{D'}$, of a cavity to the number, n, of surface elements of the cavity, and the number, N, of energy bundles traced per surface element in the MCRT model; that is,

$$Err_{D'} \leq W_c \sqrt{\frac{n-1}{Nn^2}} \tag{3.13}$$

Equation 3.13 can be used to calculate the minimum number of energy bundles required to be traced to achieve a desired global error of the distribution factors. To

establish its validity the ten numerical experiments from Section 4.3 were used to form ten matrices of distribution factors among all surface elements. For clarity, Table 4.2 shows one of the matrices as an example.

Table 4.2 establishes the convention for the distribution factors. In this case D'_{74} (= 0.039) represents the number of energy bundles emitted by surface element 7 that are absorbed in surface element 4 for numerical experiment 1, with one thousand energy bundles traced per surface element.

Table 4.2 The distribution factor matrix for numerical experiment 1 in which a thousand energy bundles are traced

j →

i ↓

	1	**2**	**3**	**4**	**5**	**6**	**7**	**8**	**9**
1	0.309	0.106	0.042	0.039	0.033	0.424	0.036	0.005	0.006
2	0.432	0.063	0.055	0.059	0.033	0.307	0.045	0.005	0.001
3	0.341	0.081	0.075	0.017	0.020	0.372	0.086	0.005	0.003
4	0.314	0.146	0.036	0.082	0.042	0.341	0.029	0.005	0.005
5	0.588	0.107	0.030	0.072	0.020	0.159	0.013	0.008	0.003
6	0.506	0.093	0.056	0.057	0.017	0.238	0.026	0.003	0.004
7	0.407	0.111	0.117	0.039	0.018	0.233	0.063	0.005	0.007
8	0.404	0.093	0.045	0.061	0.034	0.317	0.039	0.005	0.002
9	0.414	0.103	0.05	0.043	0.026	0.330	0.029	0.003	0.002

Distribution factor from surface element 7 to 4, D'_{74}

For each numerical experiment (each pair of seeds for the random number generator) the same number of energy bundles as in Section 4.2 was traced. In other words, for each numerical experiment six matrices were created for a total of sixty matrices.

After the matrices for every numerical experiment and each number of energy bundles were formed, another matrix of uncertainty was created. In this analysis the matrix of distribution factors for a hundred million energy bundles was chosen as the matrix of "true" values. Then, the matrix of errors was formed by the magnitude of the differences between the "true" value and the value for the corresponding distribution factor for the other numbers of energy bundles. Since Equation 3.13 relates the global

error, the mean of all the values on the matrix of errors was calculated. This mean was then compared to the right-hand side of Equation 3.13. Figure 4.8 shows a comparison of the mean of all the errors of the distribution factors and the corresponding value given by Equation 3.13.

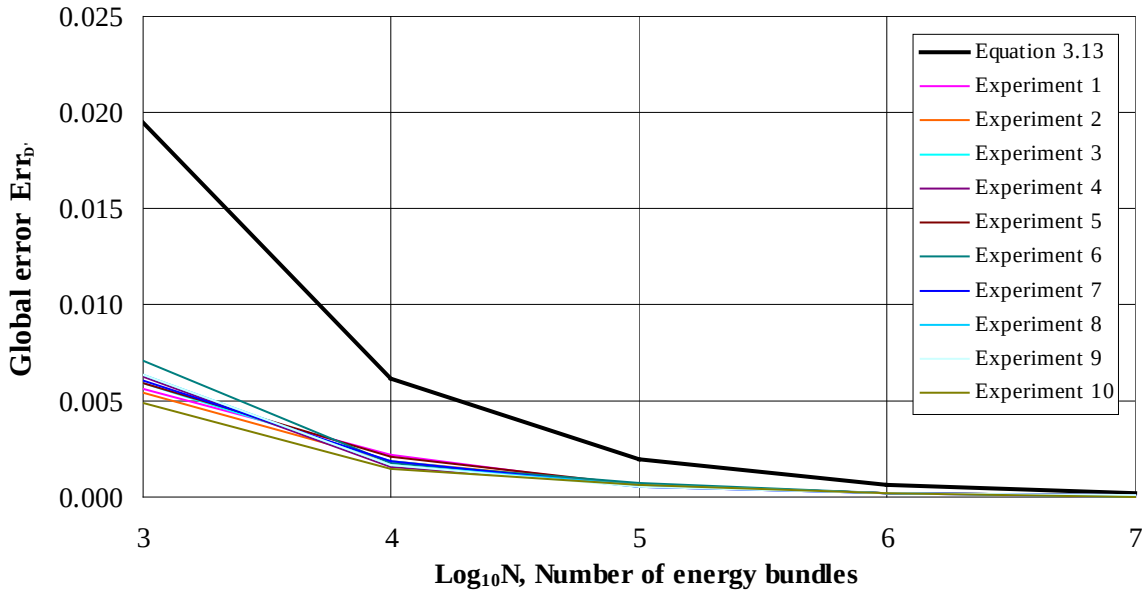

Figure 4.8 Comparison between the right-hand side of Equation 3.13 and the errors obtained from numerical experiments

The most important conclusion that can be drawn from Figure 4.8 is that Equation 3.13 indeed provides the upper bound for the observed error. In other words, the value obtained using Equation 3.13 represents the worst case for the global error in a cavity. This means that for a given number of surface elements forming an enclosure, Equation 3.13 can be used to estimate the minimum number of energy bundles required to be traced to produce a maximum permissible global error. Tables 4.3 and 4.4 show the values of the mean relative error of the distribution factor as a percentage of the mean of value of the distribution factors for the cavity for the case of 90- and 95-percent confidence intervals respectively. Recalling that $\left\langle\left\langle D'_{ij}\right\rangle\right\rangle = \frac{1}{n}$, then in this case Equation 3.13 may be written

$$\frac{\mathrm{Err}_{D'_{ij}}}{\left\langle\left\langle D'_{ij}\right\rangle\right\rangle} \le nW_c\sqrt{\frac{n-1}{Nn^2}} \tag{4.1}$$

or

$$\frac{\mathrm{Err}_{D'_{ij}}}{\left\langle\left\langle D'_{ij}\right\rangle\right\rangle} \le W_c\sqrt{\frac{n-1}{N}} \tag{4.2}$$

The right-hand side of Equation 4.2 is the same as in Equation 15.52 in Mahan [2002]. Equation 15.52 was obtained by dividing the error of the distribution factors by the estimated value of the corresponding distribution factor, and then calculating the mean of the resulting fraction. However, as pointed out earlier, it is possible to obtain a value of zero for the estimated value of the distribution factor. The current author then decided to divide the mean of the error of the distribution factor by the mean of the distribution factor (= 1/n) instead, resulting in Equation 4.2. Therefore, Table 4.4 contains the same results as Table 15.2 in Mahan [2002].

Tables 4.3 and 4.4 can be used to estimate the number of energy bundles necessary to be traced per surface element to obtain a desired relative error. It is important to emphasize that the values in Tables 4.3 and 4.4 are independent of enclosure geometry. Then, for example, we can say that in order to ensure that the mean error for the distribution factors in a 50-surface-element enclose not exceed two percent, 500,000 energy bundles would have to be traced per surface.

Table 4.3 Relative error of the distribution factors (percent) as a function of the number of surface elements, n, and the number of energy bundles traced per surface elements, N, for a 90-percent confidence level

	Number of surface elements, n														
N(10^3)	10	20	30	40	50	60	70	80	90	100	110	120	130	140	150
10	4.935	7.170	8.859	10.273	11.515	12.635	13.664	14.621	15.519	16.368	17.174	17.945	18.684	19.394	20.080
50	2.207	3.207	3.962	4.594	5.150	5.651	6.111	6.539	6.940	7.320	7.681	8.025	8.356	8.673	8.980
100	1.561	2.267	2.801	3.249	3.641	3.996	4.321	4.624	4.908	5.176	5.431	5.675	5.908	6.133	6.350
150	1.274	1.851	2.287	2.652	2.973	3.262	3.528	3.775	4.007	4.226	4.434	4.633	4.824	5.008	5.185
200	1.103	1.603	1.981	2.297	2.575	2.825	3.055	3.269	3.470	3.660	3.840	4.013	4.178	4.337	4.490
250	0.987	1.434	1.772	2.055	2.303	2.527	2.733	2.924	3.104	3.274	3.435	3.589	3.737	3.879	4.016
300	0.901	1.309	1.617	1.876	2.102	2.307	2.495	2.669	2.833	2.988	3.136	3.276	3.411	3.541	3.666
350	0.834	1.212	1.497	1.736	1.946	2.136	2.310	2.471	2.623	2.767	2.903	3.033	3.158	3.278	3.394
400	0.780	1.134	1.401	1.624	1.821	1.998	2.161	2.312	2.454	2.588	2.715	2.837	2.954	3.067	3.175
450	0.736	1.069	1.321	1.531	1.717	1.884	2.037	2.180	2.313	2.440	2.560	2.675	2.785	2.891	2.993
500	0.698	1.014	1.253	1.453	1.628	1.787	1.932	2.068	2.195	2.315	2.429	2.538	2.642	2.743	2.840
550	0.665	0.967	1.194	1.385	1.553	1.704	1.843	1.972	2.093	2.207	2.316	2.420	2.519	2.615	2.708
600	0.637	0.926	1.144	1.326	1.487	1.631	1.764	1.888	2.003	2.113	2.217	2.317	2.412	2.504	2.592
650	0.612	0.889	1.099	1.274	1.428	1.567	1.695	1.814	1.925	2.030	2.130	2.226	2.317	2.406	2.491
700	0.590	0.857	1.059	1.228	1.376	1.510	1.633	1.748	1.855	1.956	2.053	2.145	2.233	2.318	2.400
750	0.570	0.828	1.023	1.186	1.330	1.459	1.578	1.688	1.792	1.890	1.983	2.072	2.157	2.239	2.319
800	0.552	0.802	0.990	1.149	1.287	1.413	1.528	1.635	1.735	1.830	1.920	2.006	2.089	2.168	2.245
850	0.535	0.778	0.961	1.114	1.249	1.371	1.482	1.586	1.683	1.775	1.863	1.946	2.027	2.104	2.178
900	0.520	0.756	0.934	1.083	1.214	1.332	1.440	1.541	1.636	1.725	1.810	1.892	1.969	2.044	2.117
950	0.506	0.736	0.909	1.054	1.181	1.296	1.402	1.500	1.592	1.679	1.762	1.841	1.917	1.990	2.060
1000	0.494	0.717	0.886	1.027	1.152	1.264	1.366	1.462	1.552	1.637	1.717	1.794	1.868	1.939	2.008
1500	0.403	0.585	0.723	0.839	0.940	1.032	1.116	1.194	1.267	1.336	1.402	1.465	1.526	1.584	1.640
2000	0.349	0.507	0.626	0.726	0.814	0.893	0.966	1.034	1.097	1.157	1.214	1.269	1.321	1.371	1.420
2500	0.312	0.453	0.560	0.650	0.728	0.799	0.864	0.925	0.982	1.035	1.086	1.135	1.182	1.227	1.270
3000	0.285	0.414	0.511	0.593	0.665	0.730	0.789	0.844	0.896	0.945	0.992	1.036	1.079	1.120	1.159
3500	0.264	0.383	0.474	0.549	0.616	0.675	0.730	0.782	0.830	0.875	0.918	0.959	0.999	1.037	1.073
4000	0.247	0.359	0.443	0.514	0.576	0.632	0.683	0.731	0.776	0.818	0.859	0.897	0.934	0.970	1.004
4500	0.233	0.338	0.418	0.484	0.543	0.596	0.644	0.689	0.732	0.772	0.810	0.846	0.881	0.914	0.947
5000	0.221	0.321	0.396	0.459	0.515	0.565	0.611	0.654	0.694	0.732	0.768	0.803	0.836	0.867	0.898

Table 4.4 Relative error of the distribution factors (percent) as a function of the number of surface elements, n, and the number of energy bundles traced per surface elements, N, for a 95-percent confidence level

	Number of surface elements, n														
N(10^3)	10	20	30	40	50	60	70	80	90	100	110	120	130	140	150
10	5.880	8.543	10.555	12.240	13.720	15.055	16.281	17.421	18.491	19.502	20.463	21.381	22.261	23.108	23.925
50	2.630	3.821	4.720	5.474	6.136	6.733	7.281	7.791	8.269	8.721	9.151	9.562	9.956	10.334	10.700
100	1.859	2.702	3.338	3.871	4.339	4.761	5.148	5.509	5.847	6.167	6.471	6.761	7.040	7.307	7.566
150	1.518	2.206	2.725	3.160	3.542	3.887	4.204	4.498	4.774	5.035	5.284	5.521	5.748	5.966	6.177
200	1.315	1.910	2.360	2.737	3.068	3.366	3.641	3.895	4.135	4.361	4.576	4.781	4.978	5.167	5.350
250	1.176	1.709	2.111	2.448	2.744	3.011	3.256	3.484	3.698	3.900	4.093	4.276	4.452	4.622	4.785
300	1.074	1.560	1.927	2.235	2.505	2.749	2.972	3.181	3.376	3.561	3.736	3.904	4.064	4.219	4.368
350	0.994	1.444	1.784	2.069	2.319	2.545	2.752	2.945	3.125	3.296	3.459	3.614	3.763	3.906	4.044
400	0.930	1.351	1.669	1.935	2.169	2.380	2.574	2.754	2.924	3.083	3.235	3.381	3.520	3.654	3.783
450	0.877	1.274	1.573	1.825	2.045	2.244	2.427	2.597	2.756	2.907	3.050	3.187	3.319	3.445	3.567
500	0.832	1.208	1.493	1.731	1.940	2.129	2.302	2.464	2.615	2.758	2.894	3.024	3.148	3.268	3.383
550	0.793	1.152	1.423	1.650	1.850	2.030	2.195	2.349	2.493	2.630	2.759	2.883	3.002	3.116	3.226
600	0.759	1.103	1.363	1.580	1.771	1.944	2.102	2.249	2.387	2.518	2.642	2.760	2.874	2.983	3.089
650	0.729	1.060	1.309	1.518	1.702	1.867	2.019	2.161	2.293	2.419	2.538	2.652	2.761	2.866	2.968
700	0.703	1.021	1.262	1.463	1.640	1.799	1.946	2.082	2.210	2.331	2.446	2.556	2.661	2.762	2.860
750	0.679	0.987	1.219	1.413	1.584	1.738	1.880	2.012	2.135	2.252	2.363	2.469	2.571	2.668	2.763
800	0.657	0.955	1.180	1.368	1.534	1.683	1.820	1.948	2.067	2.180	2.288	2.390	2.489	2.584	2.675
850	0.638	0.927	1.145	1.328	1.488	1.633	1.766	1.890	2.006	2.115	2.220	2.319	2.415	2.506	2.595
900	0.620	0.901	1.113	1.290	1.446	1.587	1.716	1.836	1.949	2.056	2.157	2.254	2.347	2.436	2.522
950	0.603	0.877	1.083	1.256	1.408	1.545	1.670	1.787	1.897	2.001	2.099	2.194	2.284	2.371	2.455
1000	0.588	0.854	1.055	1.224	1.372	1.506	1.628	1.742	1.849	1.950	2.046	2.138	2.226	2.311	2.392
1500	0.480	0.698	0.862	0.999	1.120	1.229	1.329	1.422	1.510	1.592	1.671	1.746	1.818	1.887	1.953
2000	0.416	0.604	0.746	0.866	0.970	1.065	1.151	1.232	1.307	1.379	1.447	1.512	1.574	1.634	1.692
2500	0.372	0.540	0.668	0.774	0.868	0.952	1.030	1.102	1.169	1.233	1.294	1.352	1.408	1.461	1.513
3000	0.339	0.493	0.609	0.707	0.792	0.869	0.940	1.006	1.068	1.126	1.181	1.234	1.285	1.334	1.381
3500	0.314	0.457	0.564	0.654	0.733	0.805	0.870	0.931	0.988	1.042	1.094	1.143	1.190	1.235	1.279
4000	0.294	0.427	0.528	0.612	0.686	0.753	0.814	0.871	0.925	0.975	1.023	1.069	1.113	1.155	1.196
4500	0.277	0.403	0.498	0.577	0.647	0.710	0.767	0.821	0.872	0.919	0.965	1.008	1.049	1.089	1.128
5000	0.263	0.382	0.472	0.547	0.614	0.673	0.728	0.779	0.827	0.872	0.915	0.956	0.996	1.033	1.070

As previously stated, it is clear that Equation 3.13 provides a bound for the global error in the distribution factors. It is desirable to modify Equation 3.13 to provide an estimate of this error instead of an upper bound. The similarity in shape between the theoretical and numerical results in Figure 4.8 encouraged the author to seek a correlation that collapses the theoretical and numerical results to a single curve, which could then be expressed as

$$\mathrm{Err}_{D'_{ij}} = \mathrm{C}\mathrm{W}_c\sqrt{\frac{n-1}{Nn^2}} \tag{4.3}$$

where C is a coefficient specific to a given cavity determined by the optical properties and the geometry of the cavity. In order to accomplish this, the ratio of the mean of the experimental values to the values obtained using Equation 3.13 was formed for each number of energy bundles. Figure 4.9 shows the result of dividing the mean experimental results by the values given by the right-hand side of Equation 3.13.

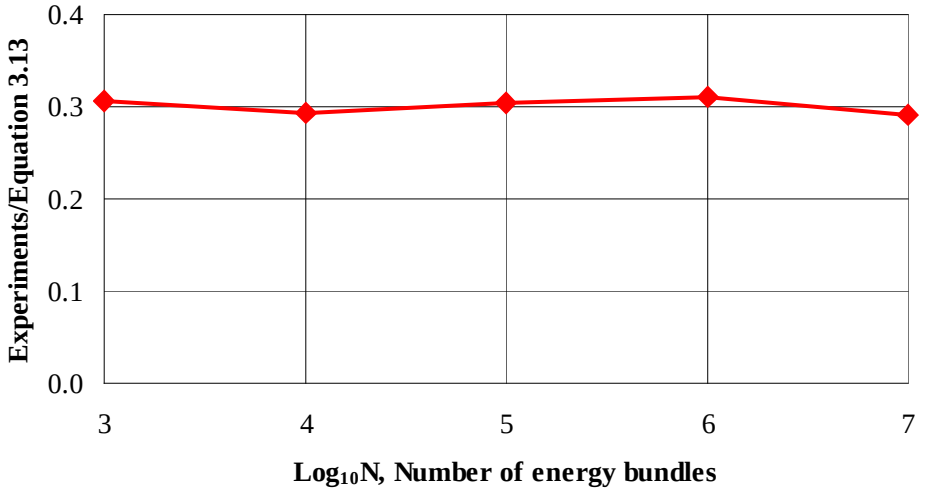

Figure 4.9 Ratio of the mean experimental results to the values given by the right-hand side of Equation 3.13 for the optical properties in Table 4.1 applied to the cavity of Figure 4.1

The mean of the fraction shown in Figure 4.9 was calculated to be approximately 0.3. Then for this specific cavity and set of surface properties, C = 0.3 and Equation 4.3 becomes

$$\mathrm{Err}_{D'_{ij}} = 0.3\,\mathrm{W}_c\sqrt{\frac{n-1}{Nn^2}} \qquad \text{(Cavity of Figure 4.1)} \tag{4.3a}$$

The values obtained using Equation 4.3a now collapse to the values obtained from the numerical experiments as demonstrated in Figure 4.10. It is clear that the modification of Equation 3.13 by a factor of 0.3 gives a very good estimate of the global uncertainty in the distribution factors. To learn more about the behavior of the coefficient C the properties of the cavity were changed and the same procedure applied to five numerical experiments, each one with different seeds for the random number generator in the MCRT. Table 4.5 contains the new values of the optical properties for the same cavity. Note that the properties of surface six now do not correspond to these of an entrance aperture. Therefore, for this particular case, surface six is treated as another mirrored wall with slightly different properties. Figure 4.11 shows the results of the ratio of the numerical experiments to the values obtained from Equation 3.13, and Figure 4.12 shows the values of the modified Equation 3.13 (Equation 4.3a) corresponding to the same numerical experiments.

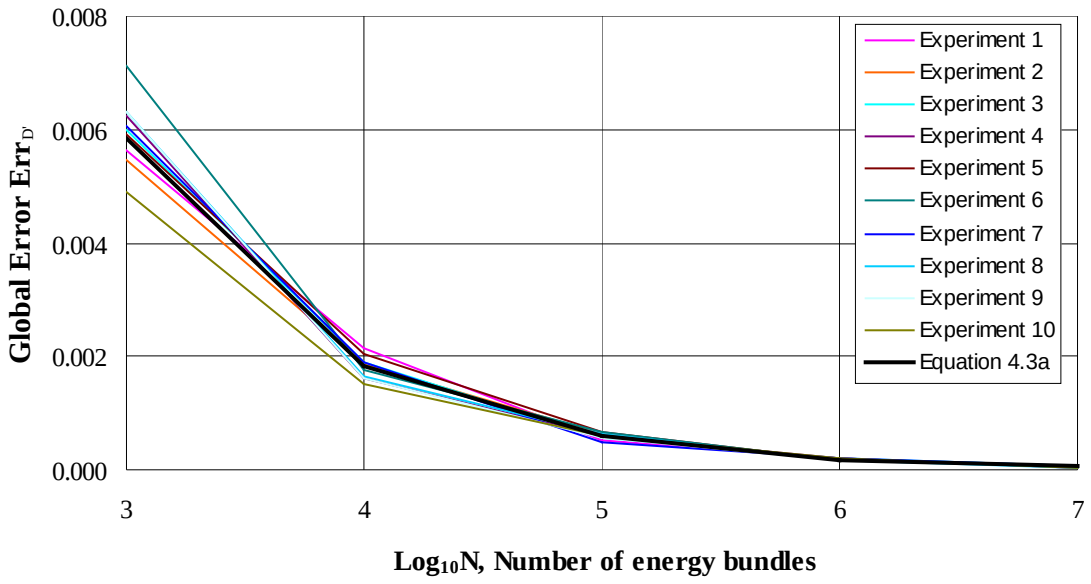

Figure 4.10 Comparison between results from Equation 4.3a (modified Equation 3.13) and results from the numerical experiments

Table 4.5 New optical properties of the cavity

Surface element number	Surface element name	Absorptivity α	Specularity ratio r_s
1	Detector	0.6	0.4
2	Mirrored wall	0.5	0.5
3	Mirrored wall	0.5	0.5
4	Mirrored wall	0.5	0.5
5	Mirrored wall	0.5	0.5
6	Mirrored wall	0.6	0.6
7	Mirrored wall	0.5	0.5
8	Mirrored wall	0.5	0.5
9	Mirrored wall	0.5	0.5

Using the optical properties from Table 4.5, the value of C is estimated to be 0.36. In this case the fraction is not as constant as in the case using the optical properties from Table 4.1. However, as shown in Figure 4.12, it can be stated that it is possible to find a coefficient C for each set of optical properties to calculate a reasonable estimate of the global uncertainty of the distribution factors. Also, considering the large differences in the values of the optical properties in the two cases considered, the values of the scaling factor, 0.3 and 0.36, are remarkably similar.

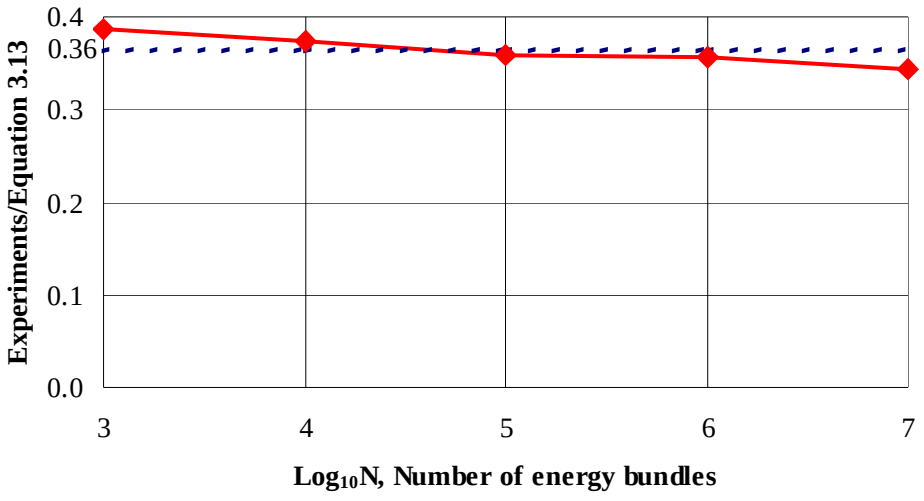

Figure 4.11 Ratio of the mean experimental results to the values given by the right-hand side of Equation 3.13, with optical properties given in Table 4.5

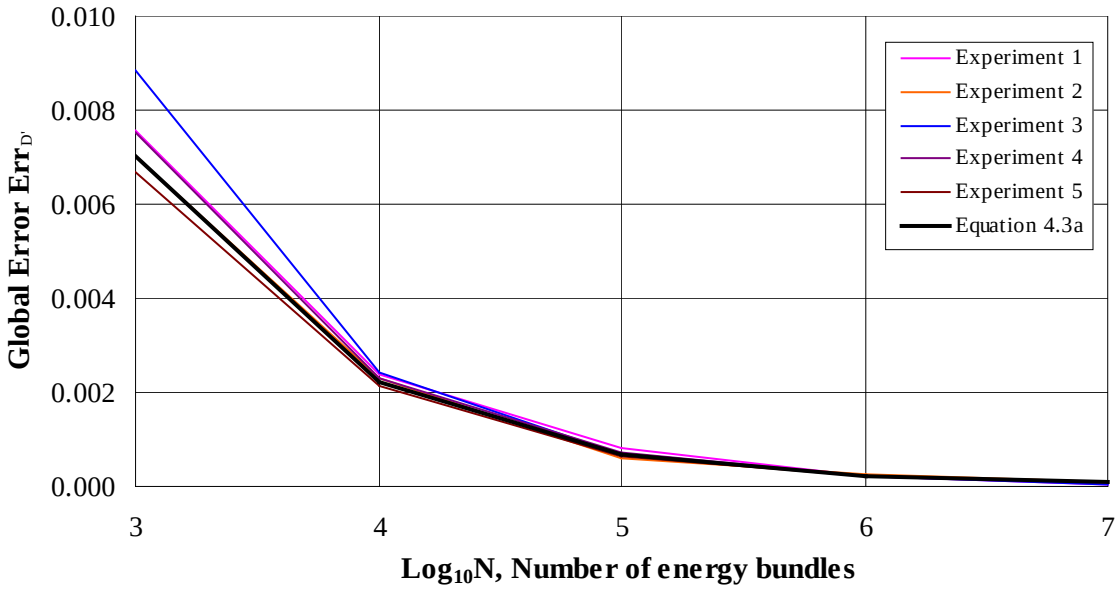

Figure 4.12 Comparison between results from the modified Equation 3.13, Equation 4.3a, and results from the numerical experiments with optical properties from Table 4.5

4.4 Validation of Equation 3.24

The approach used to establish the validity of Equation 3.24 is somewhat similar to the one used in Sections 4.3 and 4.4. For convenience in the analysis of the plots, Equation 3.24 can be written

$$\omega_{q_i'} = \varepsilon_i \sigma \sqrt{\left[\left(\frac{\omega_\varepsilon}{\varepsilon}\right)^2 + \left(\frac{4\omega_T}{T}\right)^2\right]\left[\left(T_i^4\right)^2 + \left(\sum_{j=1}^{n} T_j^4 D_{ij}'\right)^2\right] + \left[\sum_{j=1}^{n} T_j^4 \omega_{D_{ij}'}\right]^2} \qquad (4.4)$$

It is important to make clear that Equation 4.4 gives the bounds for the range of values in which the "true" and estimated values of the net heat flux should lie. Consequently, to validate Equation 3.24 its right-hand side is compared to two other quantities: (1) the values obtained for the error in the net heat flux, and (2) the uncertainty obtained from a multiple-sample numerical experiment.

The error is again defined as the difference between the "true" and estimated heat transfer. The multiple-sample numerical experiment consists of a large number of numerical estimates of the net heat flux. However, the calculation of both the "true" and estimated values as well as the numerical estimates of the net heat flux is more complex than in the case of Equations 3.5 and 3.13 because it involves the use of Equation 3.16. The following procedure, depicted also in the block diagram of Figure 4.13, was used to perform the numerical experiments for the calculation of the error based on the cavity detector of Figures 4.1 and 4.2:

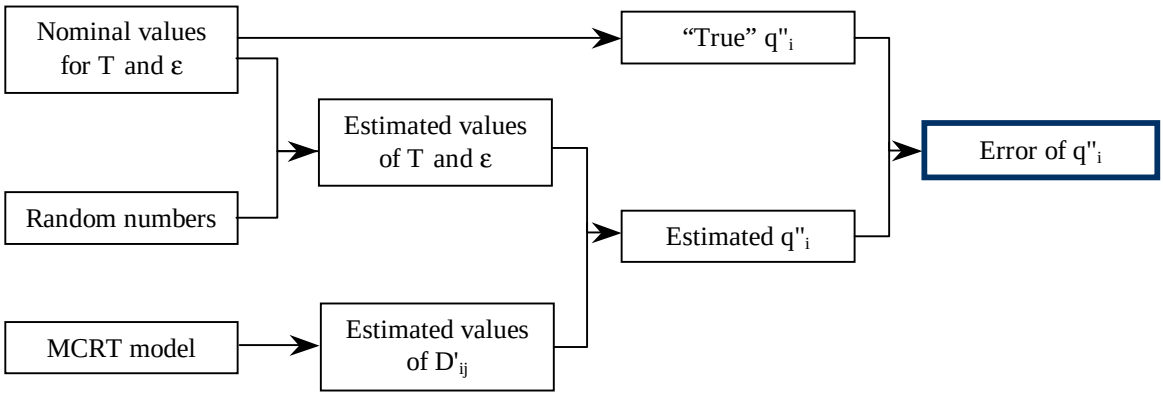

Figure 4.13 Description of the procedure used to calculate the error of the net heat flux

1. Set the values for the fractional uncertainties for the temperatures and emissivities.
2. Set the "true" values for the temperatures of each surface element of the cavity.
3. Find a "true" value for the distribution factors. In this case the values obtained by tracing one hundred million of energy bundles per surface were taken as "true" values.
4. Calculate the "true" value of the net heat fluxes using Equation 3.16,

$$q_i'' = \varepsilon_i \sum_{j=1}^{n} \sigma T_j^4 \left(\delta_{ij} - D'_{ij}\right), \qquad 1 \le i \le n \tag{3.16}$$

5. Find (random) values (from a normal distribution) for the estimated temperatures and emissivities by perturbing the "true" values according to the confidence

interval desired. The "true" temperature for each surface, T_i, is used with a normally distributed random number to generate the perturbed temperature Te_i according to

$$Te_i = T_i \cdot R(\mu, \sigma) \tag{4.5}$$

where $R(\mu,\sigma)$ is a normally distributed random number with a mean value μ and a standard deviation σ. The quantity $R(\mu,\sigma)$ is drawn from a normally distributed sequence of random numbers with a mean value of zero and standard deviation of unity using the transform

$$R(0,1) = \frac{R(\mu, \sigma) - \mu}{\sigma} \tag{4.6}$$

In this case the mean value μ is the "true" temperature value and the standard deviation is related to the fractional uncertainty by

$$\sigma = \frac{\omega_T}{Z} \tag{4.7}$$

where the value of the Z-statistic corresponds to the level of confidence associated with the fractional uncertainty. A value of 1.96, corresponding to a 95-percent confidence level, was used in all the numerical studies presented in this dissertation. The same approach was used to find values for the estimated emissivities.

6. Find the estimated distribution factors by running the MCRT with a fewer number of energy bundles than used to calculate the "true" value.
7. Calculate the estimated value of the net heat flux using Equation 3.16 with the estimated values for the temperatures, emissivities, and distribution factors.
8. Calculate the error of the net heat flux as the difference between the "true" and estimated values.

The procedure shown in the block diagram of Figure 4.14 was used to obtain the numerical estimates of the net heat flux for the calculation of the uncertainty

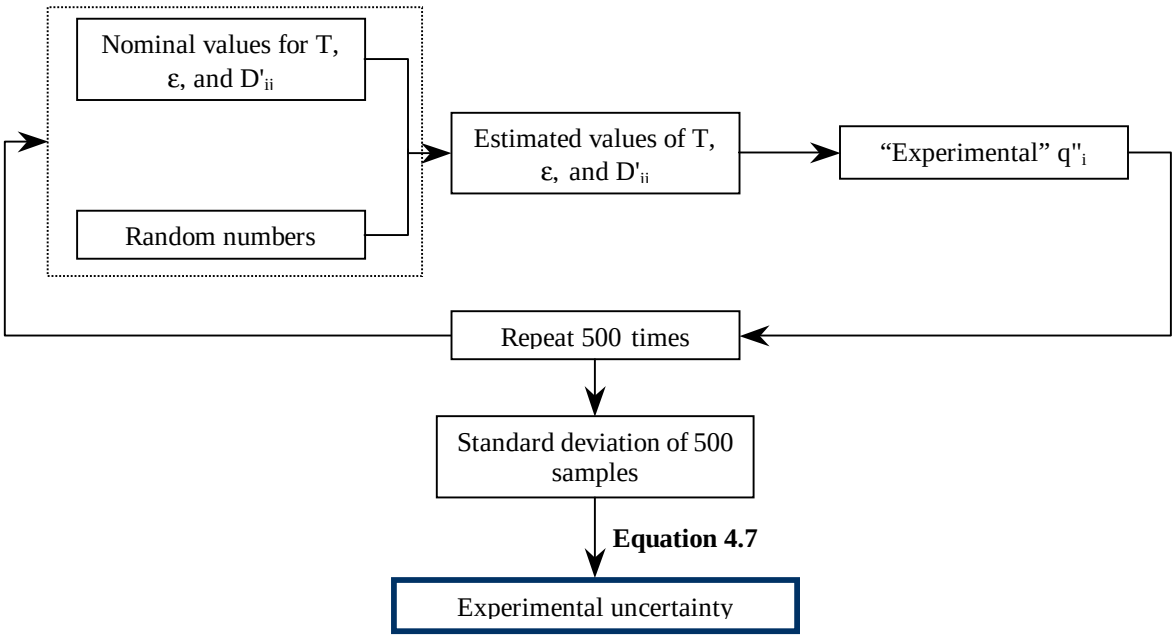

Figure 4.14 Description of the procedure used to calculate the uncertainty of the net heat flux

1. Follow Steps 1 through 3 of the procedure for the estimation of the error.
2. Perturb the "true" distribution factors using the same methodology explained in Step 5 of the procedure for the estimation of the error. Use the right-hand side of Equation 3.13 (global uncertainty of the distribution factors) to calculate the value of the uncertainty in Equation 4.7.
3. Calculate the value of the net heat flux using Equation 3.16 and the values of the estimated temperatures, emissivities, and distribution factors obtained in Steps 1 and 2.
4. Repeat Steps 1 through 3 for a large number of samples using a different set of random numbers each time.
5. Calculate the standard deviation of the distribution obtained and then calculate the uncertainty using Equation 4.7.

After estimating the "experimental" error and the "experimental" uncertainty have been estimated, these quantities are compared with the right-hand side of Equation 4.4 determined using estimated values for temperatures and distribution factors and the

values for the fractional uncertainties established in Step 1. The process is repeated for three different sets of seeds for the random number generator.

Note that this case involves four degrees of freedom: optical properties, temperature distribution, number of energy bundles traced, and fractional uncertainties. A study of all these parameters was performed. In previous studies [Sánchez, 1998; Sánchez *et al.*, 1999, 2000, 2001] it has been shown that the number of energy bundles traced is the parameter that has the most impact on the results of this kind of numerical experiment. Therefore all the following analyses are performed tracing different numbers of energy bundles.

4.4.1 Contribution of estimated temperatures and emissivities to the error in the net heat flux

To study the contribution of estimated temperatures and emissivities to the error in the net heat flux, it is necessary to change the set of seeds of the random number generator to produce statistically independent values of the error and the right-hand side of Equation 4.4. Since Equation 4.4 is used for one specific surface, all the studies were performed for surface 1, the detector, which is the critical surface in this application. One "true" temperature distribution was set and the values of the fractional uncertainty of the temperature and emissivity were both maintained constant at 0.002 (0.2 percent). Three different sets of seeds are used to produce three sequences of random numbers, which are used to obtain the estimated temperature distributions, giving three independent numerical experiments. The same sequences are also used to generate five hundred values of the net heat flux using steps 1 through 5 explained in the previous section, each value using different random number of the sequence. The different values of the net heat flux are then used to calculate the experimental uncertainty. Table 4.6 gives the values of the optical properties and the temperature distribution used for this set of numerical experiments. Figure 4.15 shows the effect of changing the seeds on the calculation of the statistical uncertainty of five hundred samples of the net heat flux.

Table 4.6 Optical properties and temperatures of the surface elements of the cavity in Figures 4.1 and 4.2 used in Section 4.4.1

Surface element number	Surface element name	Temperature K	Absorptivity α	Specularity ratio r_s
1	Detector	305	0.9	0.1
2	Mirrored wall	314	0.1	0.9
3	Mirrored wall	313	0.1	0.9
4	Mirrored wall	313	0.1	0.9
5	Mirrored wall	305	0.1	0.9
6	Entrance aperture	310	1.0	NA
7	Mirrored wall	305	0.1	0.9
8	Mirrored wall	305	0.1	0.9
9	Mirrored wall	308	0.1	0.9

It is important to say that in Figure 4.15 and all the figures in the rest of this chapter, lines between the point values are provided to aid the readability of the trends. Also note that the x-axis of theses figures is a logarithmic scale.

First, note that the three curves are almost identical. This means that the effect of the different estimated temperature and emissivity distributions in the uncertainty is minor. Remember that the only difference between the three numerical experiments is the set of seeds used in the random number generator to calculate the estimated temperature and emissivity distributions.

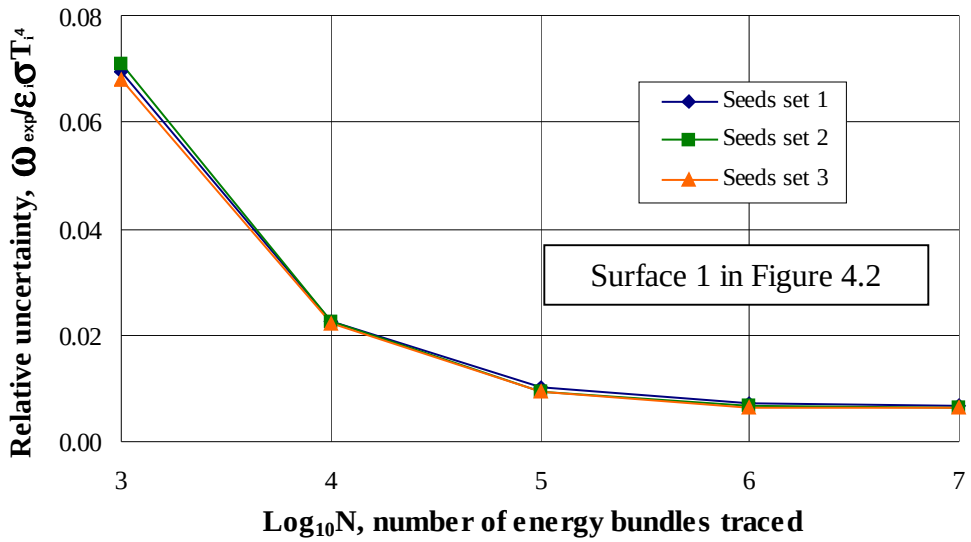

Figure 4.15 Statistical uncertainty of three sets of five hundred samples of the net heat flux, each set having different seeds of the random number generator to create the sequences of random number as explained in Steps 1 through 5 in page 58

Figure 4.16 shows the case for the uncertainty calculated using the right-hand side of Equation 3.24. Recall that Equation 3.24 is Equation 4.4 divided by the term $\varepsilon_i\sigma_i T_i^4$. Again, the seeds of the random number generator were changed to obtain three different distributions of estimated temperature and emissivity as explained on Steps 1 through 8 on page 56 and 57.

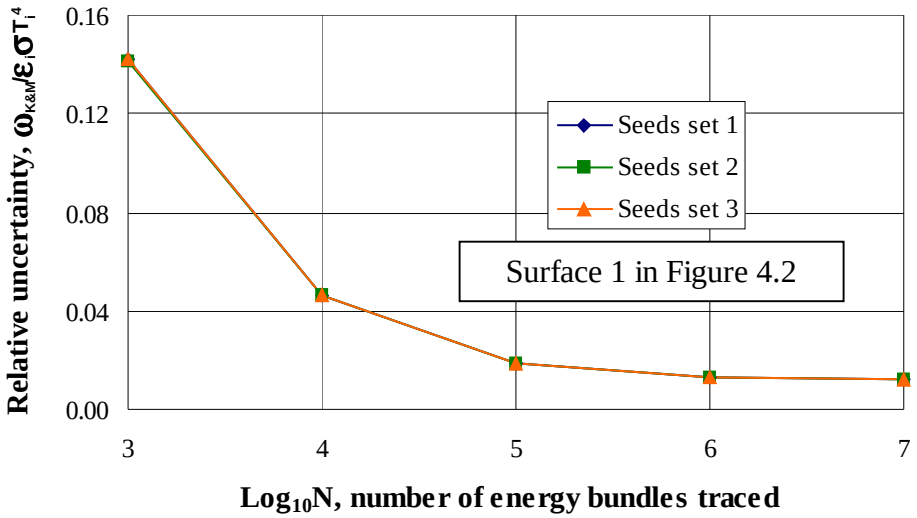

Figure 4.16 Uncertainty calculated using the right-hand side of Equation 3.24 for three different sets of seeds of the random number generator used to obtain the estimated temperature and emissivity distributions as explained in Steps 1 through 8 on pages 56 through 57

The three curves of Figure 4.16 are essentially identical. This means that the uncertainty based on the formalism of Kline and McClintock is not affected by changes of the distribution of the estimated temperature and emissivity within the range considered.

Figure 4.17 shows the effect of the different sets of seeds of the random number generator on the error. For comparison, the three curves of the error are shown with one curve of the experimental uncertainty and one of the uncertainty calculated using the Kline and McClintock approach. Note that the vertical axis is now a logarithmic scale.

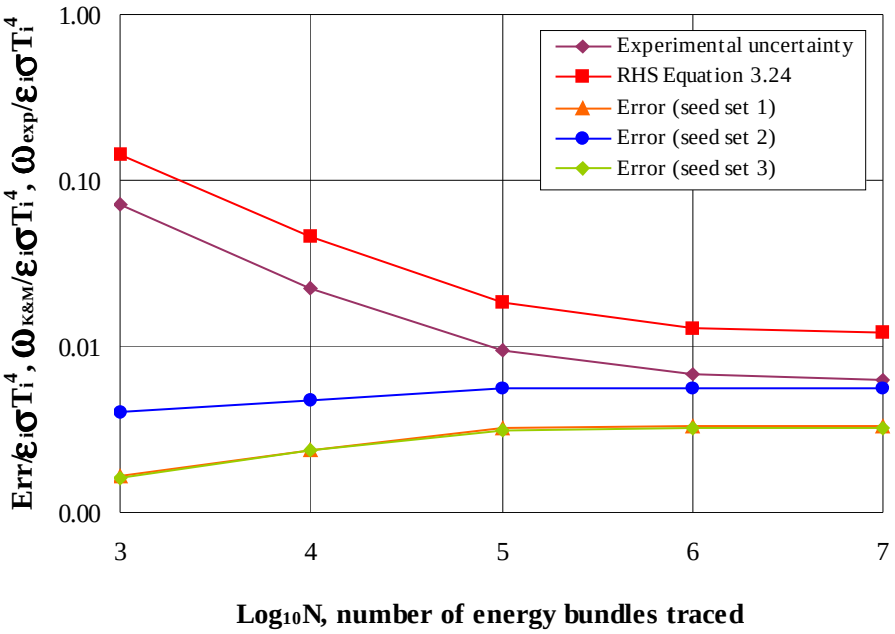

Figure 4.17 Error of the net heat flux for three different sets of seeds of the random number generator

In the case of the error, Figure 4.17 shows that it is more sensitive to changes in the estimated temperature and emissivity than the uncertainty. The variability among these curves is explained by the effect of the fourth power on the temperatures, which is more explicit in the calculation of the error than in the uncertainty. Note that the uncertainty obtained using the Kline and McClintock formalism agrees well with the experimental uncertainty predicted by the five hundred sample numerical experiment. The relative uncertainty predicted by Equation 3.24 is generally greater than the experimental uncertainty. One possible explanation for this is that, while the numerical experiment provides a good estimate of the uncertainty, it cannot provide its exact value because a finite number of samples is used. Also, as expected, both uncertainties (experimental and from Kline and McClintock) bound the error.

It is important to make clear that in Figures 4.15 through 4.17 the only parameter that changes in each experiment is the set of seeds for the random number generator, and that the fractional uncertainty of the temperatures and emissivities are held constant at 0.002. Changing the seeds of the random number generator provokes changes in the values of the estimated temperature and emissivity distributions. Also recall that the same

sets of seeds are used to create the 500 sets of values of the net heat flux, which are used to calculate the experimental uncertainty.

4.4.2 Contribution of the "true" temperature distribution to the error and uncertainty of the net heat flux

To study the effect of the true temperature distribution of the surface elements in the cavity of Figure 4.1 on Equation 3.24, three more "true" temperature distributions were randomly created to form four different range of values (311 to 313 K, 305 to 315 K, 300 to 400 K and 200 to 500 K). The first two ranges are realistic for an actual cavity radiometer element, while the last two are extreme. Then the resulting heat flux and its error and uncertainty were compared to those values obtained using the temperature distribution of Section 4.4.1. Table 4.7 shows the values of the temperature distributions used in this set of numerical experiments. The fractional uncertainties of the temperature and emissivity, ω_T/T and $\omega_\varepsilon/\varepsilon$, have been maintained constant at 0.002 in this study.

In the previous section numerical experiment number two seemed to be the experiment that produced values very different from those of the other two experiments. For this reason the seeds of the random number generator from numerical experiment number two were used to generate the estimated temperature distributions in this study. Figure 4.18 shows the values obtained for the error, the Kline and McClintock uncertainty (right-hand side of Equation 3.24), and the experimental uncertainty of the net heat flux for the four "true" temperature distributions from Table 4.7.

Table 4.7 Temperature distributions on the walls of the cavity shown in Figures 4.1 and 4.2 used in Section 4.4.2

Surface element number	Surface element name	Temperature distribution 1 (K)	Temperature distribution 2 (used in Section 4.4.1) (K)	Temperature distribution 3 (K)	Temperature distribution 4 (K)
1	Detector	312.51	305	384	402
2	Mirrored wall	312.32	314	371	258
3	Mirrored wall	310.33	313	312	403
4	Mirrored wall	310.16	313	345	262
5	Mirrored wall	310.08	305	389	246
6	Entrance aperture	312.05	310	365	372
7	Mirrored wall	311.89	305	359	239
8	Mirrored wall	312.77	305	324	455
9	Mirrored wall	310.89	308	396	278

The most important feature of Figure 4.18 is that the relative uncertainty predicted by Equation 3.24 consistently provides an upper bound for the experimental uncertainty, which in turn also bounds the error. This is important because it implies that Equation 3.24 gives a conservative estimate of the maximum relative uncertainty of the net heat flux of a surface in an enclosure for a given temperature distribution. Note that the difference between the experimental uncertainty and the uncertainty predicted by the Kline and McClintock formalism decreases significantly as the number of energy bundles increases. One can reasonably assume that for an infinite number of energy bundles traced this difference would converge to zero.

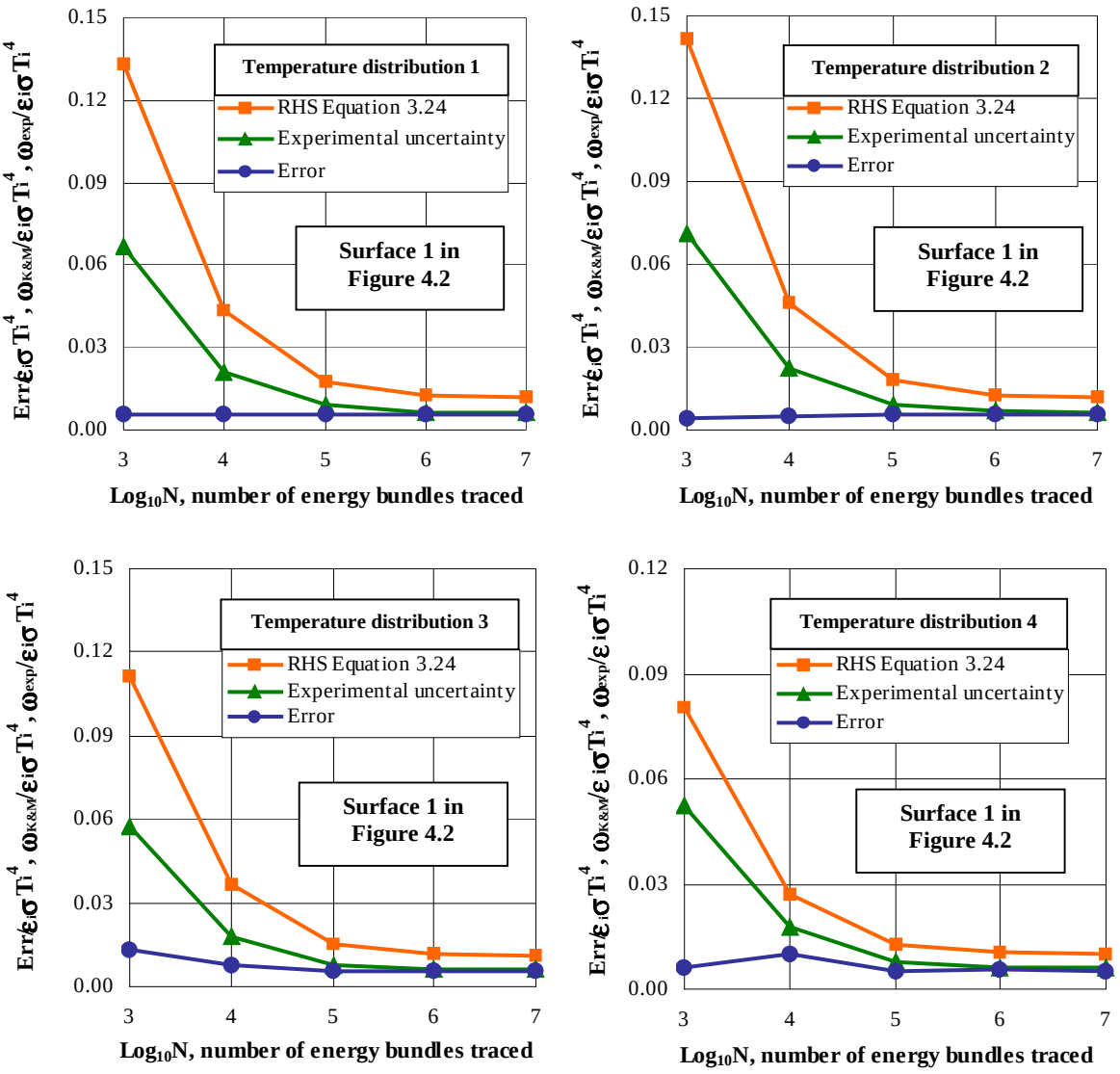

Figure 4.18 Comparison of the error, experimental uncertainty, and the uncertainty calculated using the Kline and McClintock formalism, for "true" temperature distributions 1, 2, 3, and 4 from Table 4.7

An important observation from Figure 4.18 is that the shape of the curves is very similar in all four plots. This implies that changes in the "true" temperature distribution affects both sides of Equation 3.24 to almost the same degree. Also, as expected, all of the plots show that the experimental uncertainty is greater than the error all the time. It is also important to note that for sufficiently large number of energy bundles it can be concluded that the Kline and McClintock uncertainty of the net heat flux, $\omega_{K\&M}$, is an

adequate estimate of the experimental uncertainty and the error. It is interesting to note that the error remains relatively constant for all "true" temperature distributions and number of energy bundles traced.

From Figure 4.18 it appears that the magnitude of the relative uncertainty predicted by Equation 3.24 and the experimental uncertainty decreases as the temperature range increases, i.e. the temperature distribution is less isothermal. However, care should be taken when interpreting this result because the values of the uncertainties are normalized by the term $\varepsilon_i \sigma T_i^4$ where T_i is the temperature of the surface under consideration (in this case, surface 1). In the four cases presented the temperature for each surface was assigned randomly within a range, with a range increasing from temperature distribution 1 to temperature distribution 4. However, the temperature of surface 1 is generally greater as the range of temperatures increases, and since this temperature is used in the normalization term, a higher temperature resolves in a lower normalized uncertainty.

4.4.3 Contribution of the fractional uncertainty in Equation 3.24

To study the influence of the fractional uncertainties in Equation 3.24, new numerical experiments were run with different values for the fractional uncertainty in the temperature and emissivity. Temperature distribution number 2 in Table 4.6 was used for these numerical experiments and, again, the set of seeds for numerical experiment number 2 was used to generate the estimated temperature and emissivity distributions. The results for these experiments are shown in Figures 4.19 with values for both the fractional uncertainty in the temperature, ω_T/T, and emissivity, $\omega_\varepsilon/\varepsilon$, of 0.02, 0.002, and 0.0002 respectively.

(a)

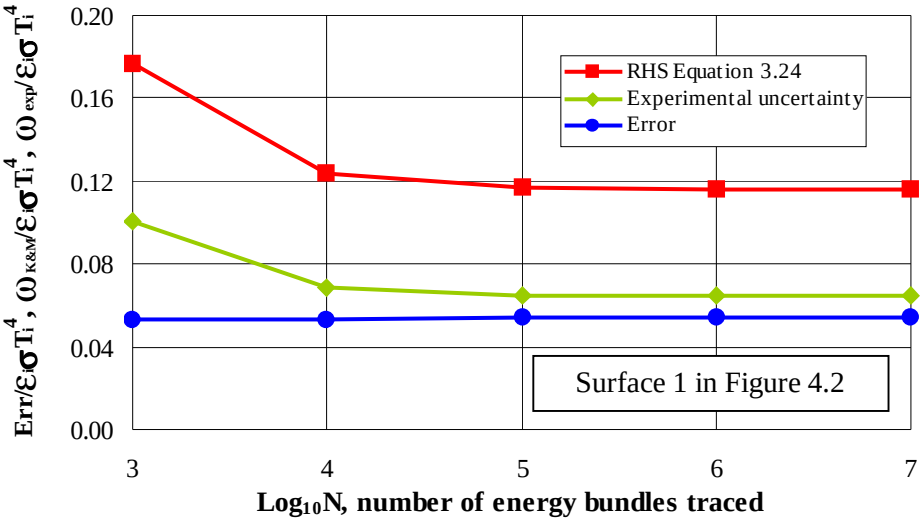

(b)

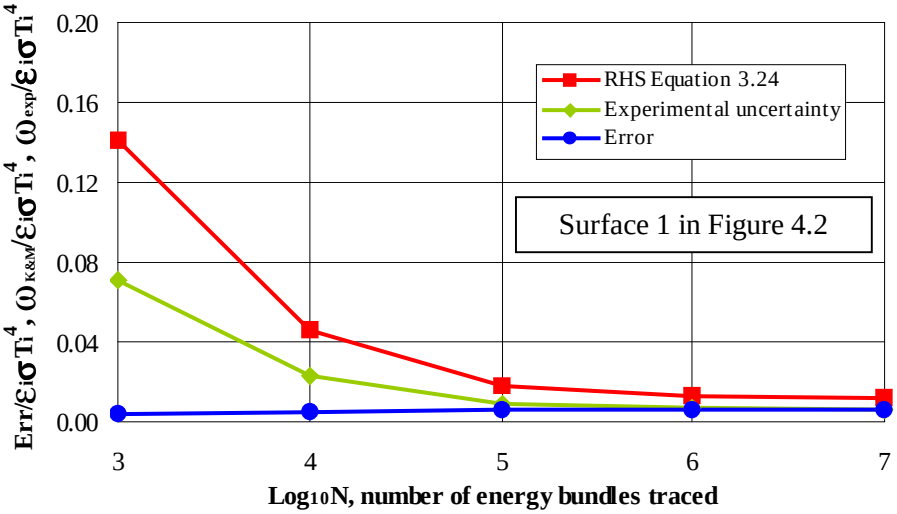

(c)

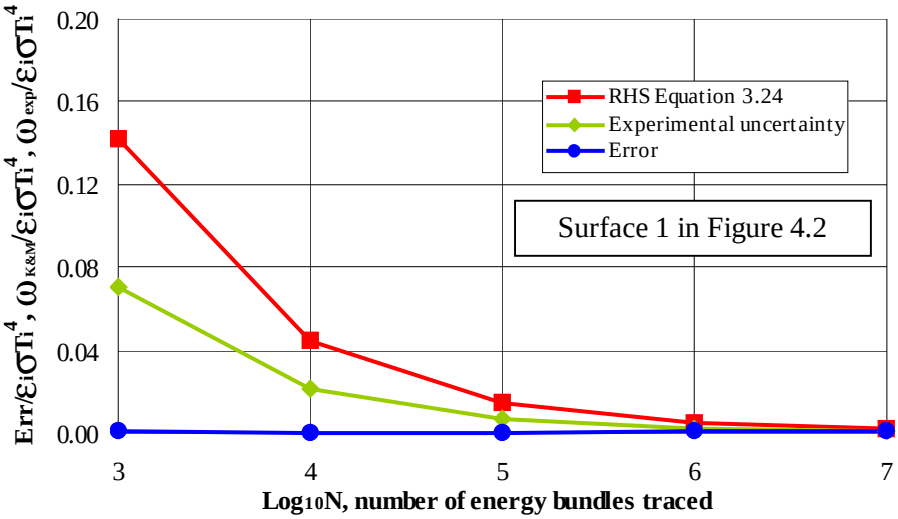

Figure 4.19 Comparison of the error, experimental uncertainty, and the uncertainty calculated using Kline and McClintock formalism (right-hand side of Equation 4.4), for fractional uncertainty of temperature and emissivity of (a) 0.02, (b) 0.002, (c) 0.0002

It can be seen from Figure 4.19 that the uncertainty predicted by Equation 3.24 always has a greater value that the experimental uncertainty and the error. Again, this indicates that Equation 3.24 provides an upper bound for the relative uncertainty.

The uncertainty predicted by Equation 3.24 converges to a finite value that is a function of the uncertainty of the emissivity, temperature, and distribution factor. For each case presented in this study the uncertainty of emissivity and temperature are fixed, while the uncertainty of the distribution factor is a function of the energy bundles traced. For the case where the uncertainty in emissivity and temperature are much grater than the uncertainty of the distribution factor, as in case (a) in Figure 4.19, the uncertainty predicted using the Kline and McClintock formalism (Equation 3.24) converges quickly to a value that is much greater than the value of the experimental uncertainty. In contrast, for the second case, case (b) in Figure 4.19, the uncertainty predicted by the Kline and McClintock formalism converges to a value slightly greater than the experimental uncertainty. Likewise, for the third case, case (c) in Figure 4.19, the uncertainty predicted by the Kline and McClintock formalism appears to converge to the same value as the experimental uncertainty. A possible explanation of this trend is that in case (a) the dominant term in Equation 3.24 is the term containing the fractional uncertainty of emissivity and temperature. In case (b) the term containing the fractional uncertainty of emissivity and temperature and the term containing the uncertainty of the distribution factor both have a significant influence on the predicted uncertainty. In case (c) the dominant term in Equation 3.24 is the term containing the uncertainty of the distribution factor.

In the studies presented in this section it has been demonstrated that Equation 3.24, obtained using the Kline and McClintock formalism, provides a predicted relative uncertainty of the net heat flux of a surface in an enclosure that is consistently greater than the “experimental” uncertainty obtained from the numerical experiments for several different cases. This implies that Equation 3.24 provides an upper bound of the relative uncertainty of the net heat flux independent of the temperature distribution or values of the uncertainty of temperature and emissivity.

4.5 Validation of Equation 3.39

Equation 3.39 is purported to provide an upper bound of the global relative uncertainty in the net heat flux of the cavity as a function of (1) the number of energy bundles traced, (2) the number of surface elements into which the enclosure is divided, and (3) the temperature distribution of the enclosure. Once again, Equation 3.39 can be written

$$\left\langle \left(\frac{\omega_{q_i''}}{\varepsilon_i \sigma T_i^4} \right) \right\rangle_i^2 \leq \left[\left(\frac{\omega_\varepsilon}{\varepsilon} \right)^2 + \left(\frac{4\omega_T}{T} \right)^2 \right] \left[1 + n^2 \frac{\left\langle T^4 \right\rangle^2}{\left\langle \left(T^4\right)^2 \right\rangle} \right] + \frac{W_c^2}{N} \left(1 - \frac{1}{n} \right) \tag{3.39}$$

To validate this equation, it is necessary to prove that the right-hand side provides a bound for the global relative error of the net heat transfer. To do this, the temperature distributions 1, 2, and 3 created in Section 4.4.2 were used as the basis for numerical experiments. The error in the net heat flux was calculated using steps 1 through 8 of the process outlined for numerical experiments at the beginning of Section 4.4. After the error of the net heat flux was estimated, the mean of all the errors was compared to the right-hand side of Equation 3.39. To calculate the global experimental uncertainty of the net heat flux of all the surfaces of the cavity, the net heat flux of each surface was estimated five hundred times with different estimated temperature and emissivity distributions and different distribution factors, all estimated as explained in Section 4.4. Then the uncertainty of these net heat fluxes was computed and finally the mean of the uncertainties was obtained. The results of the study are divided according to the parameter observed, as in Section 4.4.

4.5.1 Contribution of the estimated temperatures and emissivities in Equation 3.39

The first parameters studied are the estimated temperatures and emissivities. For this study all variables are kept constant except for the set of seeds of the random number generator, which are changed three times to produce three different estimated temperature

and emissivity distributions. Each of these three different distributions of estimated temperature and emissivity are used with the estimated distribution factors (at $N < 10^8$) to calculate an estimated value of the net heat flux from each surface in the enclosure as explained in Steps 1 through 7 on page 57. A "true" value of the net heat flux from each surface in the enclosure is calculated with the nominal values of the temperature and emissivity and the "true" values of distribution factors ($N = 10^8$). The mean relative uncertainty of the net heat flux is calculated using the right-hand side of Equation 3.39 and the estimated values of the temperatures, emissivities, and distribution factors. The mean error of the net heat flux is then calculated as the difference of the mean of estimated relative heat fluxes and the mean of the "true" relative heat fluxes.

The mean of the experimental uncertainty of the heat flux is estimated by generating a large number (five hundred) of numerical estimates of the heat flux from each surface in the enclosure and then calculating the uncertainty of the heat flux of each surface. Each estimate of the heat flux is obtained by perturbing the nominal values of the temperature, emissivity, and distribution factors using different random numbers as explained on page 58. Three different random number seeds are used to create three different sets of five hundred estimated heat fluxes, which are then used to provide three different estimates of experimental uncertainty. The x-axis of all the graphs contains the number of energy bundles traced to estimate the distribution factors and to compute the right-hand side of Equation 3.39. The fractional uncertainty for this set of numerical experiments in the temperature and emissivity is 0.002, and temperature distribution number 2 from Table 4.7 of Section 4.4.2 was used as the "true" temperature.

Figure 4.20 shows the curves of the experimental uncertainty for the three different sets of seeds of the random number generator.

From Figure 4.20 it is possible to conclude that the different temperature and emissivity distributions have little effect on the global relative uncertainty of the net heat flux. A good feature of the figure is that the global relative uncertainty tends to go to zero as the number of energy bundles increases. This means that the distribution factors play the dominant role in the estimation of the global experimental uncertainty.

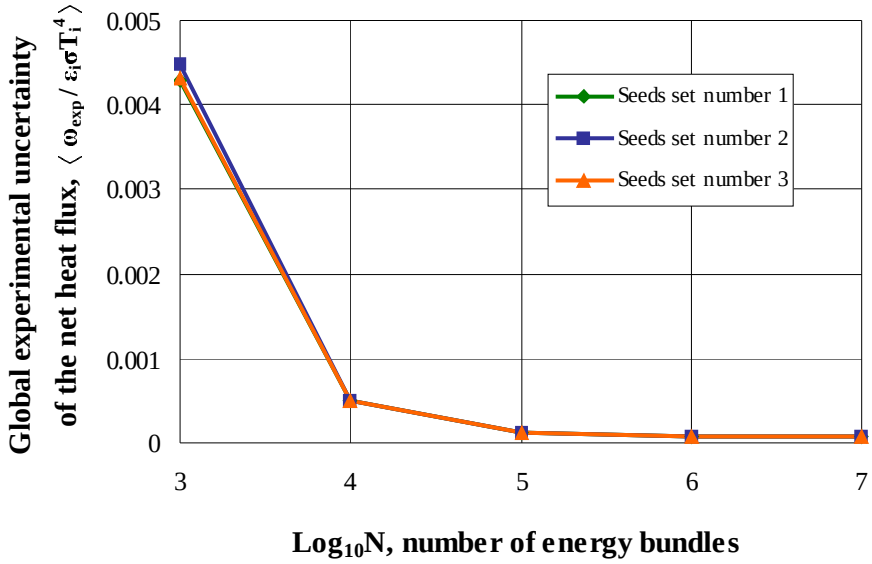

Figure 4.20 Global relative experimental uncertainty of the net heat flux for three different sets of seeds of the random number generator used to obtain different temperature and emissivity distributions

Figure 4.21 shows the effect of changing the seeds of the random number generator to obtain the estimated temperature and emissivity distribution on the right-hand side of Equation 3.39. Again, changing the seeds of the random number generator has no effect on the global relative uncertainty of the relative net heat flux as calculated using the Kline and McClintock formalism. Looking in a detailed manner to the right-hand side of Equation 3.39, this can be explained because the effect of having different estimated temperatures is eliminated by the ratio of the means of the temperatures, which, for the temperature distributions studied, is always very close to unity. Also, the dominant term is the square of the number of surfaces, n, kept constant in the study reported in this section.

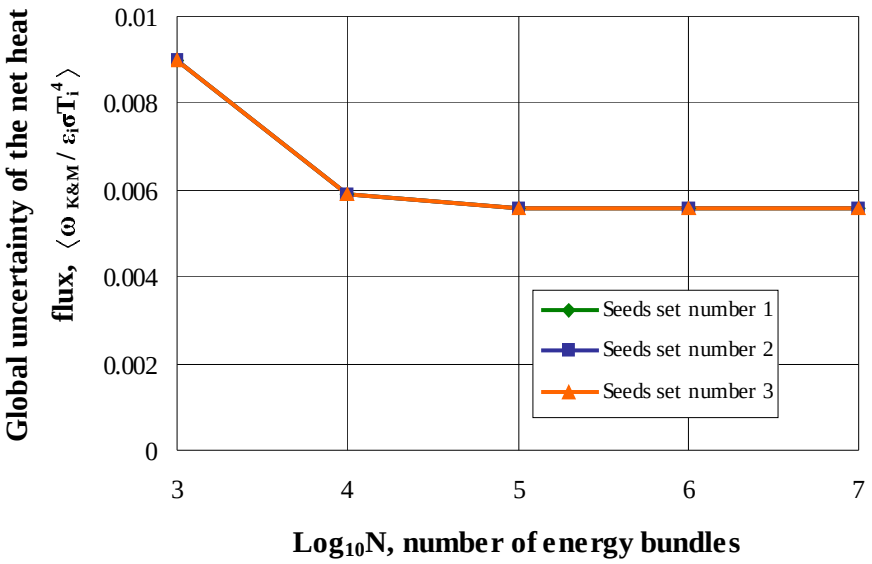

Figure 4.21 Global uncertainty of the net heat flux calculated using the Kline McClintock formalism (right-hand side of Equation 3.39) for three different sets of seeds of the random number generator used to obtain different temperature and emissivity distributions

Finally, the three curves of the global error of the net heat flux are shown in Figure 4.22. Note in Figure 4.22 that, in contrast to the relative uncertainty, the global relative error of the net heat flux is somewhat affected by changes in the estimated temperature and emissivity distributions. As it was the case in Section 4.4.1, these changes in the error of the net heat flux can be explained by the fourth power of the temperatures, which produces considerable differences between "true" and estimated temperatures.

For comparison, the three curves of the global relative error of the net heat transfer were plotted in Figure 4.23 along with the curve of the right-hand side of Equation 3.39 corresponding to the seeds set 2 and the curve of the experimental uncertainty corresponding also to the seeds set 2.

From Figure 4.23 it is possible to deduce that for a fractional uncertainty of 0.002, the right-hand side of Equation 3.39 is a very conservative method to bound the global relative error of the net heat flux and a somewhat conservative bound of the experimental uncertainty. Observe again that, as expected, the global relative experimental uncertainty of the net heat flux always bounds its global relative error.

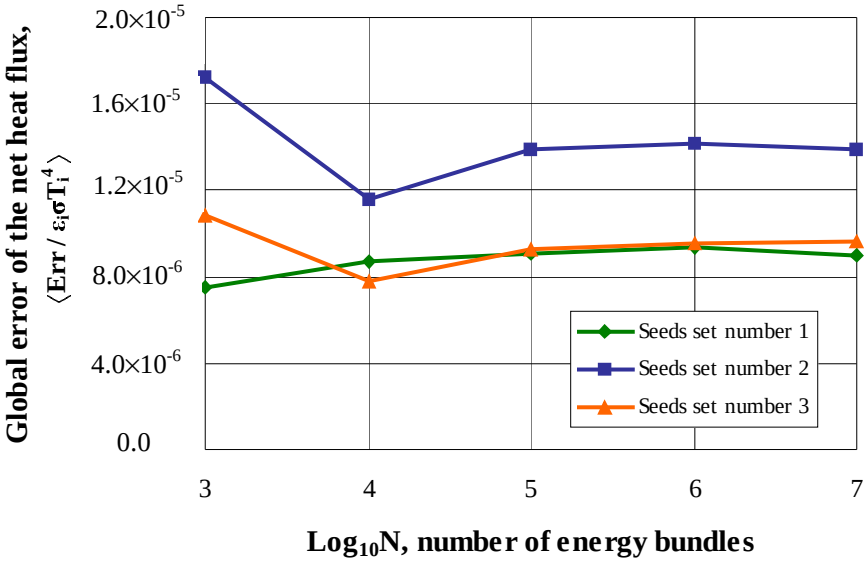

Figure 4.22 Global relative error of the net heat flux for three different sets of seeds of the random number generator used to obtain different temperature and emissivity distributions

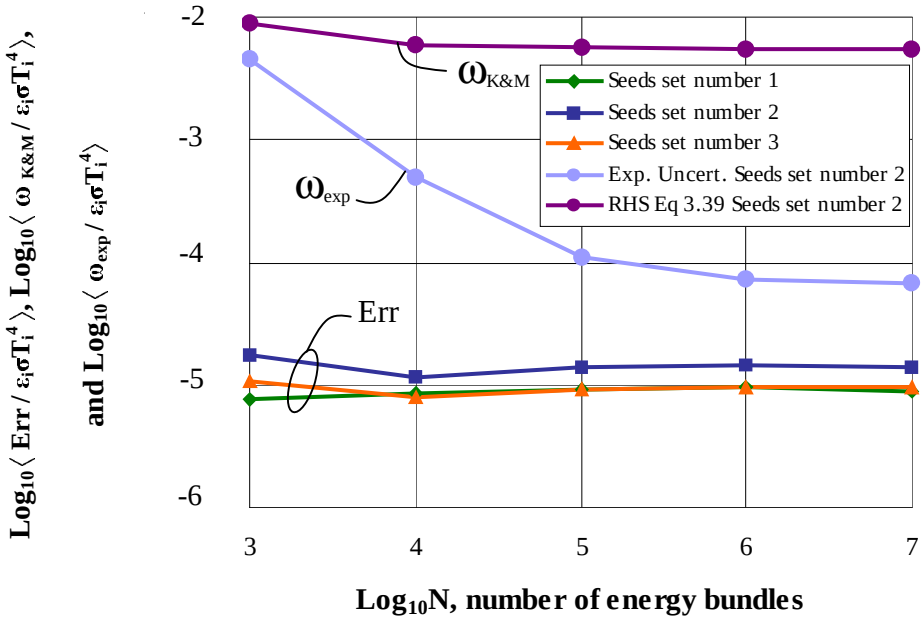

Figure 4.23 Comparison between the right-hand side of Equation 3.39, the experimental global relative uncertainty, and three curves of the global relative error of the net heat flux for fractional uncertainty of 0.002 and "true" temperature distribution 2 from Table 4.7

4.5.2 Contribution of the fractional uncertainty in Equation 3.39

For this part of the study, temperature distribution 2 was again used as the "true" set of temperatures and the second set of seeds for the random number generator was again used. The different values of the fractional uncertainty in temperature and emissivity used were (1) 0.02, (2) 0.002, and (3) 0.0002. Figure 4.24 shows the results.

Interesting conclusions can be drawn from Figure 4.24. First, it is important to note that both the right-hand side of Equation 3.39 and the experimental global relative uncertainty provide an upper bound on the global relative error in each of the three sets of experiments. Also, note that the values of the global relative uncertainty from Kline and McClintock (right-hand side of Equation 3.39), the relative error and the experimental global relative uncertainty decrease as the value of the fractional uncertainty decreases.

Note in Figure 4.24 that in each set of experiments, the behavior of the Kline and McClintock uncertainty and the relative error is very similar, and the difference between them remains fairly constant. However the changes of the experimental uncertainty follow a different trend than the other two curves. Note that as the fractional uncertainty decreases, the experimental global uncertainty of the net heat flux gets closer to the Kline and McClintock uncertainty and diverges from the error. This means that the smaller the fractional uncertainty, the better approximation of the global relative uncertainty of the net heat flux can be obtained using the right-hand side of Equation 3.39. If the values of the fractional uncertainty are small compared to the range of the surface temperatures, the relative uncertainty of the net heat flux is also small and strongly dependent on the number of energy bundles traced. If the values of the fractional uncertainty are large compared to the range of temperatures, the global relative uncertainty of temperature dominates in the numerical experiments and the uncertainty of the net heat flux varies very little with the number of energy bundles. Therefore, it can be concluded that for small values of the fractional uncertainty (compared with the percentage difference between minimum and maximum temperatures in the temperature distribution), Equation 3.39 can be a useful guide to choosing the number of energy bundles used to achieve a desired global relative uncertainty of the net heat flux.

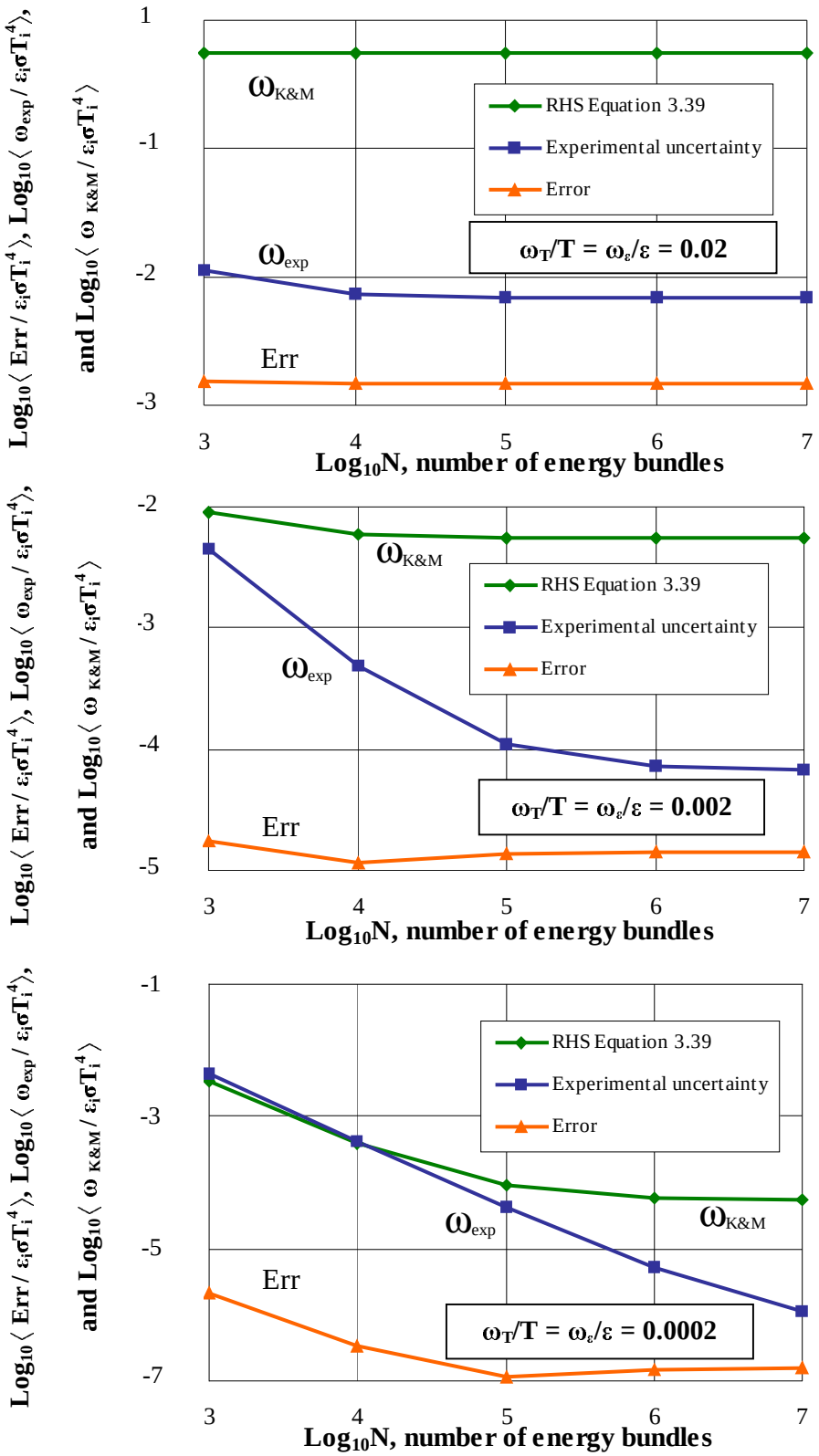

Figure 4.24 Comparison of the global relative error, experimental global relative uncertainty, and global relative uncertainty calculated using Kline and McClintock theorem (right-hand side of Equation 3.39), for fractional uncertainty of temperature and emissivity of (1) 0.02, (2) 0.002, (3) 0.0002

4.5.3 Effect of the "true" temperature distribution in Equation 3.39

"True" temperature distributions 1, 2, 3, and 4 from Table 4.7 in Section 4.4.2 were used to study the effect of the "true" temperature distribution on the global relative uncertainty in the net heat flux. Figure 4.25 shows the curves for the global uncertainty from Kline and McClintock and the experimental uncertainty (right-hand side and left-hand side of Equation 3.39) using the four temperature distributions. The fractional uncertainty of the temperature and emissivity were kept constant at 0.002 and the second set of seeds for the random number generator were used to create the estimated temperature and emissivity distributions, as explained in Section 4.4.

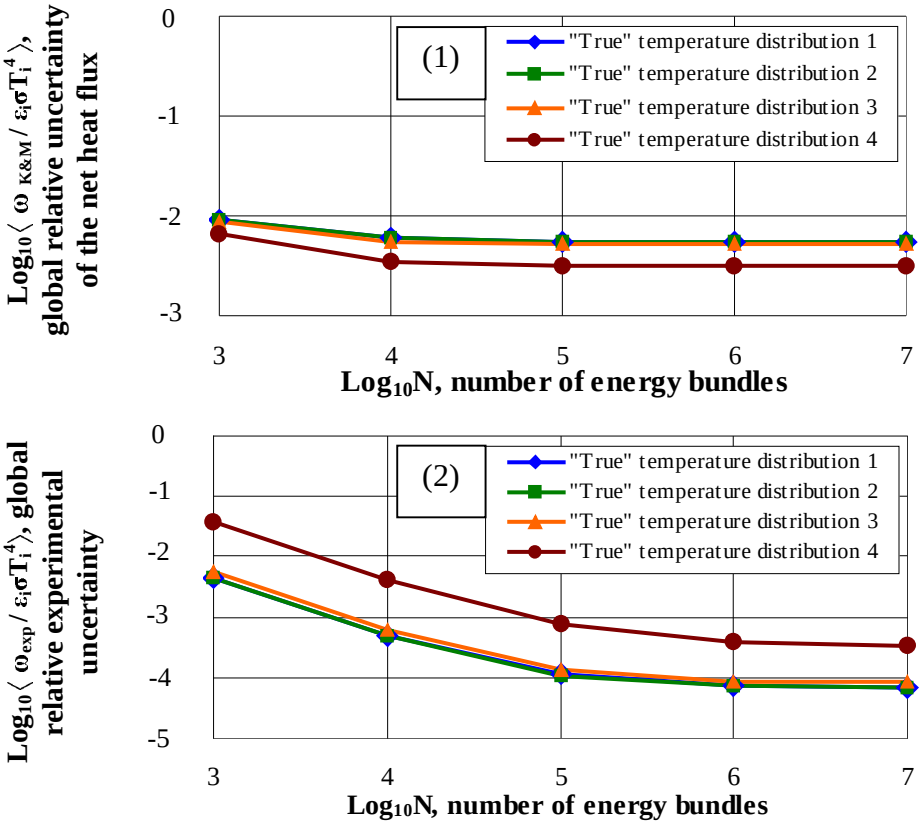

Figure 4.25 Global relative uncertainty of the net heat flux obtained from (1) Kline and McClintock and (2) numerical experiments

Figure 4.25 show that as the range of the "true" temperature increases, the value of the uncertainty obtained using the Kline and McClintock theorem decreases, while the value of the experimental uncertainty increases. The values of both uncertainties seem to be relatively close for "true" temperature distributions 1, 2, and 3, but "true" temperature distribution 4 appears to affect significantly the uncertainties. A deeper analysis is necessary to draw any conclusion. Figure 4.26 show the values of both uncertainties and the error for "true" temperature distribution 1 and 4 and fractional uncertainty 0.002

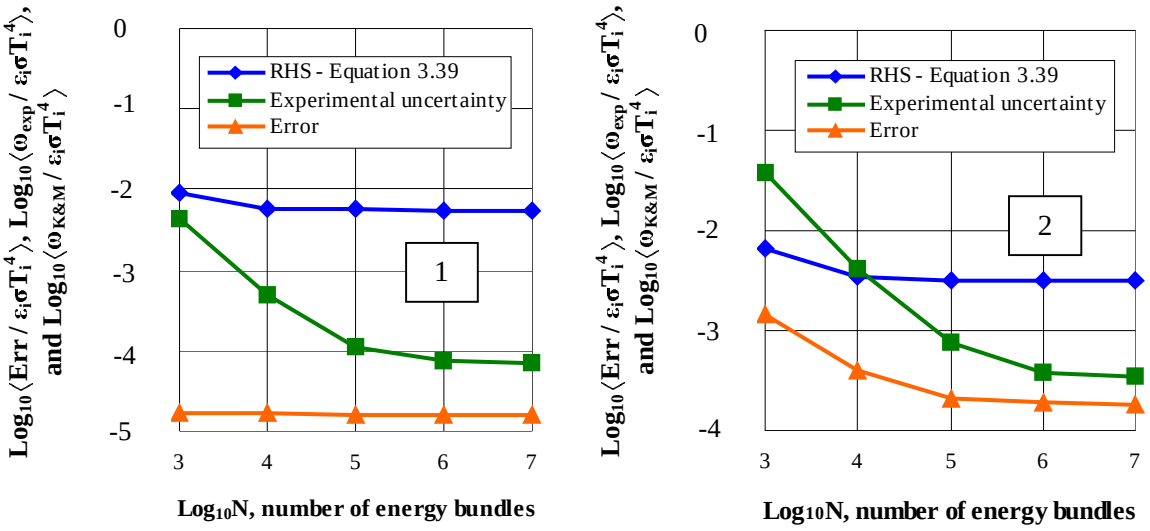

Figure 4.26 Comparison between the global relative uncertainty of the net heat flux from Kline and McClintock (right-hand side Equation 3.39), the global experimental relative uncertainty and the global relative error for fractional uncertainty of 0.002 and (1) "true" temperature distribution 1 (2) "true" temperature distribution 4

Note that for this value of fractional uncertainty Figure 4.26 shows that "true" temperature distribution 4 produces values that make Equation 3.39 invalid for a certain range of numbers of energy bundles. However, the experimental relative uncertainty always bounds the relative error, as expected. To understand more the behavior using the "true" temperature distribution 4, the global relative uncertainties and error are plotted again using this distribution with different values of fractional uncertainty. The same parameters are also plotted using "true" temperature distribution 1 for comparison. Figure 4.27 show the results for fractional uncertainty of 0.02, and Figure 4.28 show the results with a fractional uncertainty of 0.0002.

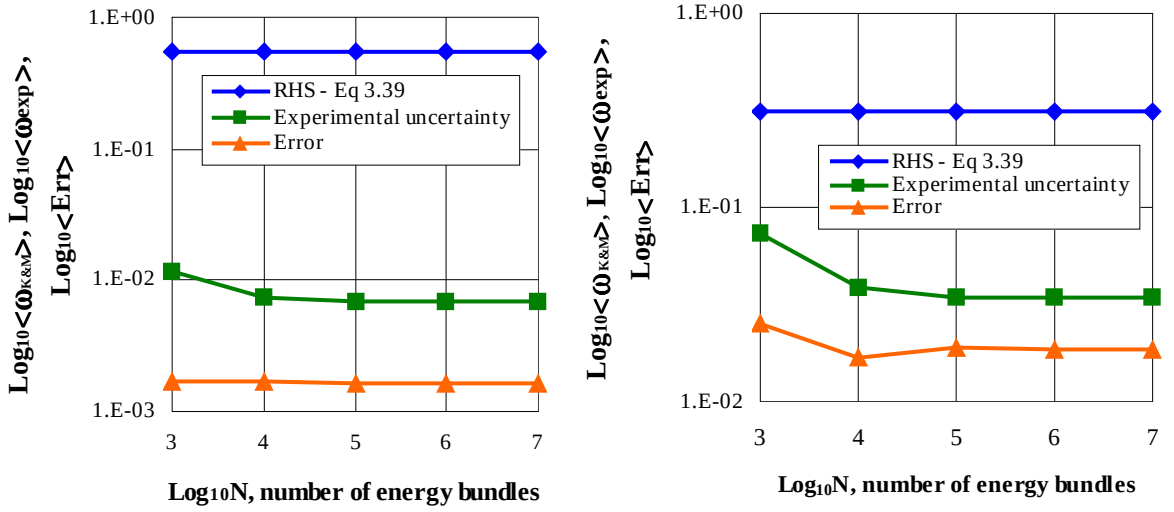

Figure 4.27 Comparison between the global uncertainty of the net heat flux from Kline and McClintock (right-hand side Equation 3.39), the global experimental uncertainty and the global error for fractional uncertainty of 0.02 and (1) "true" temperature distribution 1 (2) "true" temperature distribution 2

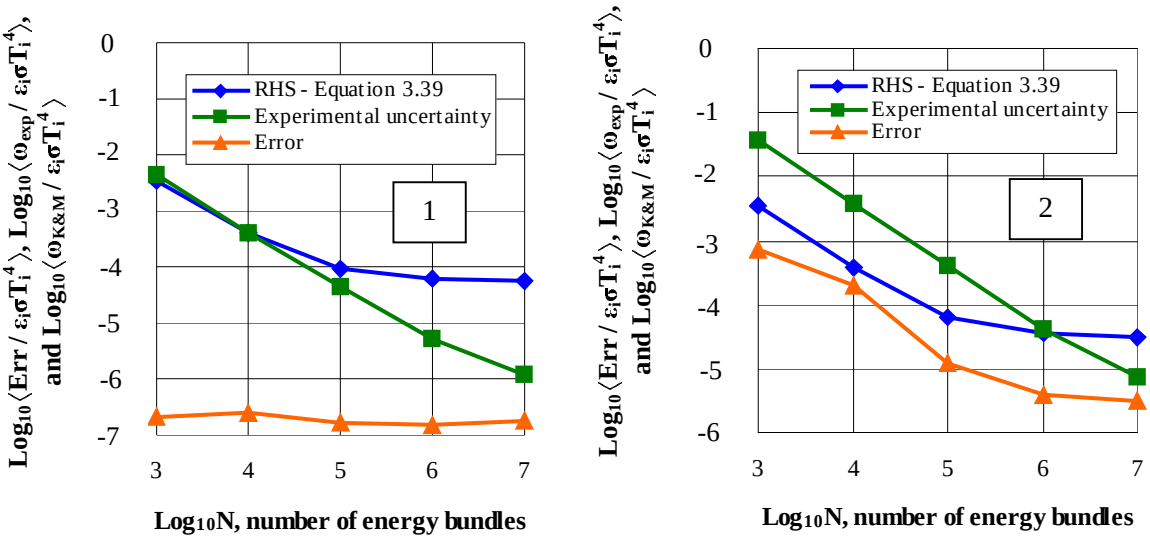

Figure 4.28 Comparison between the global relative uncertainty of the net heat flux from Kline and McClintock (right-hand side Equation 3.39), the global experimental relative uncertainty and the global relative error for fractional uncertainty of 0.0002 and (1) "true" temperature distribution 1 (2) "true" temperature distribution 4

Figures 4.26 through 4.28 reveal a somewhat unexpected trend. For a temperature distribution having a large range of temperatures ("true" temperature distribution 4 has a range of temperatures of 200 to 500 K), as the fractional uncertainty decreases, the right-hand side of Equation 3.39 fails to accurately predict the global uncertainty of the net heat transfer. However, for a small range of temperatures ("true" temperature distribution 1 has a range of 311 to 313), when the fractional uncertainty decreases, Equation 3.39 produces a better estimation of the global uncertainty of the net heat flux. The physical significance of this trend is unclear. Since a better approximation of the uncertainty should be obtained when the fractional uncertainty decreases, the fact that with large ranges of temperatures this is not true, caution should be used when it is desired to use Equation 3.39 to predict the global relative uncertainty of the heat flux of an enclosure with a large range of surface temperatures.

4.6 Effect of the number of surfaces on Equations 3.13 and 3.39

The only parameter left to study is the number of surface elements into which the enclosure has been divided. Equations 3.13 as well as Equation 3.39 represent functions of the number of surfaces elements. To study the effect of the number of surface elements on the global uncertainty of distribution factors and net heat flux, another model of the same cavity studied in the previous sections was used. In this section the same cavity is now modeled with only three surface elements: the entrance aperture, the detector, and the rest of the cavity combined into one single surface element. Table 4.8 gives the values of the properties and temperature distributions of the surface elements for this new enclosure.

Table 4.8 Optical properties and temperature distributions used in Section 4.6

Surface element number	**Surface element name**	**Absorptivity α**	**Specularity Ratio r_s**	**Temperature distribution 1 K**	**Temperature distribution 2 K**	**Temperature distribution 3 K**
1	Detector	0.9	0.1	311.21	309	336
2	Entrance aperture	1	1	312.51	305	313
3	Cavity	0.1	0.9	312.05	310	390

Figure 4.29 shows the comparison between three numerical experiments and Equation 3.13 using this model of the cavity. The reader is reminded that the three numerical experiments differ only in that different sets of seeds were used to generate the sequence of random numbers used.

For comparison, three values of the global error (corresponding to experiments 1,2, and 3 from Figure 4.8) and the values of the global uncertainty (right-hand side Equation 3.13) for the nine-surface cavity are plotted in Figure 4.29 along with the values for the three experiments for the three-surface cavity. Note that the numerical experiments demonstrate the counter-intuitive result that the global uncertainty of the distribution factors increases as the number of surface elements decreases. However, it is clear that Equation 3.13 continues to provide an upper bound for the global uncertainty of the distribution factors in the cavity.

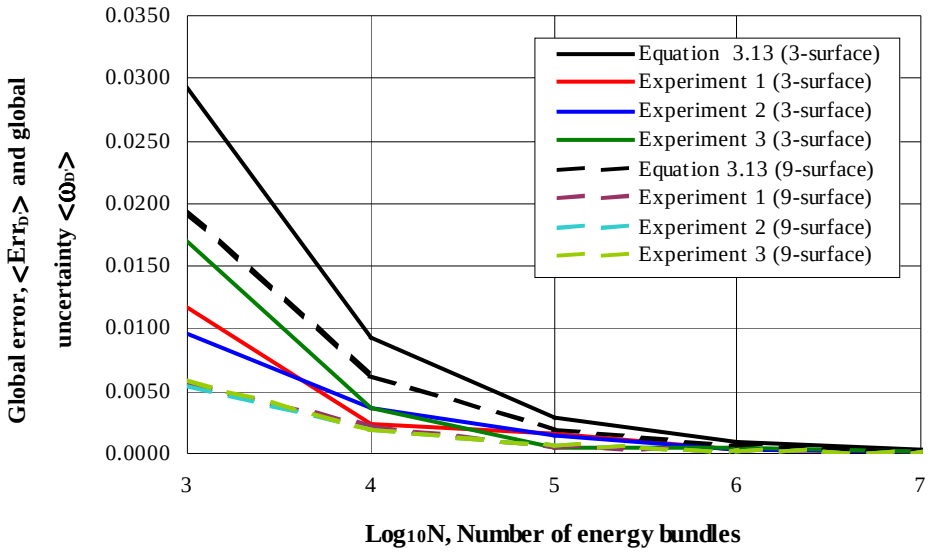

Figure 4.29 Comparison between Equation 3.13 and three numerical experiments for the cavity of Figures 4.1 and 4.2 now defined by three surface elements

It is now desired to make an attempt to collapse the curves for the global error of the distribution factors (left-hand side of Equation 3.13) to the curves of the global uncertainty of the distribution factors (right-hand side Equation 3.39) by finding a factor that would transform the inequality of Equation 3.13 into Equation 4.3, as it was done in

Section 4.3. Again, the mean of the values of the global error of the numerical experiments was divided by the values obtained using the right-hand of Equation 3.13. Figure 4.30 shows the values of this ratio.

Figure 4.30 shows that for the three-surface cavity the ratio of the numerical experiments to the values obtained with Equation 3.13 is not as constant as the ratio obtained with the nine-surface cavity when the number of energy bundles traced change. The mean of the ratio showed in Figure 4.30 was calculated to be approximately 0.41 and it is represented by the dashed line in the same figure. Then, for the three-surface cavity Equation 4.3 becomes

$$\mathrm{Err}_{D'_{ij}} = 0.41\, W_c \sqrt{\frac{n-1}{Nn^2}} \qquad \text{(3 surface cavity)} \qquad (4.5)$$

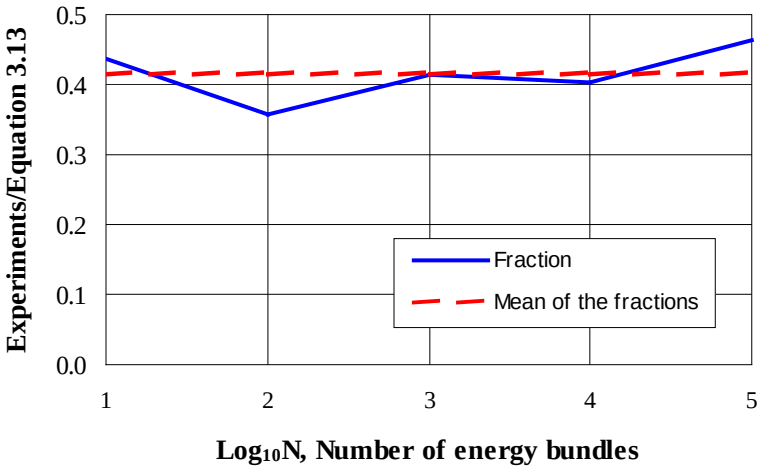

Figure 4.30 Ratio of the experimental results to the values obtained using the right-hand side of Equation 3.13 for the three-surface cavity and the optical properties of Table 4.11

The same model of the cavity was used for the study of the effect of the number of surface elements in Equation 3.39. The "true" values for the temperature distributions were obtained by using the same temperatures for the entrance aperture and the detector as those in Table 4.7 in Section 4.4.2, and the mean of the temperatures of the remaining surfaces for the temperature of the cavity. These values are shown in Table 4.8. The fractional uncertainty of the temperature and emissivity were kept constant at 0.002.

Figure 4.31 shows a plot of the global uncertainty and error in the net heat flux for the three temperature distributions given in Table 4.8 using Equation 3.39 for the three-surface cavity. The figure shows that Equation 3.39 provides a conservative bound for the uncertainty in the net heat flux. The three curves for the right-hand side overlap each other, indicating that the temperature distribution has little effect on the relative uncertainty in net heat flux for this cavity. The same thing can be said about the global relative experimental uncertainty. Note that the values of the uncertainty are smaller for this cavity than those for the nine-surface cavity showed in Figure 4.26. This figure seems to indicate that with fewer surfaces the "true" temperature distributions have less effect on the global uncertainty. However a more complete analysis with different geometries would be required to validate this statement.

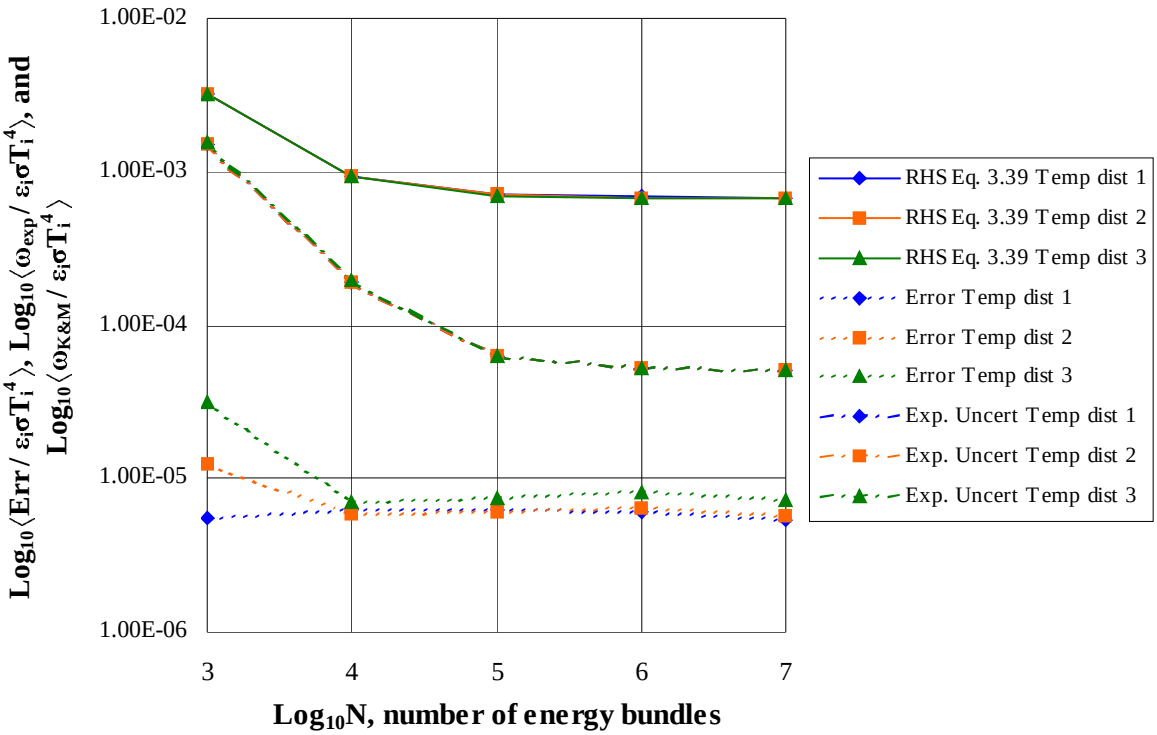

Figure 4.31 Comparison between the global relative uncertainty from Kline and McClintock (right-hand side of Equation 3.39), the global experimental relative uncertainty and the global relative error of the net heat transfer for temperature distribution 1, 2, and 3 from Table 4.8 and fractional uncertainty of temperature and emissivity of 0.002

The numerical experiments whose results are given in Figure 4.24 also show that after ten thousand energy bundles have been traced the global error of the net heat flux for the cavity with 3 surfaces is no longer sensitive to the increment of the energy bundles.

All pertinent parameters in Equations 3.5, 3.13, 4.4, and 3.39 have been studied as well as the effect of these parameters in such equations. In the next chapter, an example application of the use of these equations is presented. Specifically a model for the CERES instrument is used as the enclosure for which the uncertainty in the distribution factors and net heat flux is predicted.